



Selective furfural conversion via parallel hydrogenation–oxidation on MOF-derived CuO/RuO₂/C electrocatalysts via pulsed laser

Shreyanka Shankar Naik^{a,1}, Jayaraman Theerthagiri^{a,1}, Ahreum Min^{b,1}, Cheol Joo Moon^{b,1}, Seung Jun Lee^{c,1}, Myong Yong Choi^{a,b,*}

^a Department of Chemistry (BK21 FOUR), Research Institute of Natural Sciences, Gyeongsang National University, Jinju 52828, Republic of Korea

^b Core-Facility Center for Photochemistry & Nanomaterials, Gyeongsang National University, Jinju 52828, Republic of Korea

^c Department of IT-Energy Convergence (BK21 FOUR), Korea National University of Transportation, Chungju 27469, Republic of Korea

ARTICLE INFO

Keywords:

Pulsed laser ablation
Metal–organic frameworks
CuO/RuO₂/C
Overall water splitting
Furfural oxidation and hydrogenation reactions

ABSTRACT

Herein, Cu-metal–organic framework-derived CuO/C and CuO/RuO₂/C were fabricated via pulsed laser ablation and calcination, demonstrating multifunctional electrocatalytic performances toward hydrogen and oxygen evolution, furfural hydrogenation, and oxidation reactions (HER, OER, FHR, and FOR) in alkaline solution. CuO/RuO₂/C showed a high HER activity with 127-mV overpotential and 98.4-mV/dec Tafel slope. In contrast, during FHR, CuO/C converted 14.93-mM furfural to furfuryl alcohol (FFA) in 120-min with a Faradaic efficiency (FE) of 80.12 %, demonstrating a high yield. Similarly, CuO/RuO₂/C showed a high OER activity with lowest overpotential ~346-mV; subsequently, adding 50-mM furfural reduced that to 1.536 V vs. RHE. Furthermore, during FOR, furfural conversion was highly-favorable to achieve furoic acid (FA) upto 13.28-mM with a FE ~77.56 % and C-balance of ~77.56 %. Moreover, CuO/C||CuO/RuO₂/C electrolyzer was fabricated to simultaneously convert furfural into FA and FFA, saving-energy with enhanced-efficiency. Finally, in situ/operando electrochemical-Raman spectroscopy revealed the surface reorientation and M^{III}-O intermediate formation during HER and OER.

1. Introduction

Valorizing biomass into value-added chemicals is highly beneficial and productive owing to increased energy consumption and dependency on petrochemical resources worldwide [1,2]. For several decades, converting natural extracts/products into industrially viable chemicals has been studied to retain the carbon balance (CB) in the ecosystem. Among several biomass-derived materials, furfural (FF) is regarded as a promising intermediate owing to its versatile nature to convert platform chemicals into valuable intermediate, including furfuryl alcohol (FFA), methyl furan, cyclopentanone, 2-furoic acid (FA), cyclopentanol, and tetrahydrofurfuryl alcohol, etc., via oxidation and hydrogenation. Among these, FA and its derivatives are considered excellent feedstock intermediates used in pharmaceutical products, fungicides, and perfumes [3–5]. Further, the hydrogenation of FF to FFA is important because FFA is the primary monomer employed in synthesizing furan-based resins. In addition, FFA is one of the pivotal intermediate

compounds for producing dyes, pharmaceutical ingredients, rocket fuel, rubber, and agricultural products [6,7]. Therefore, converting FF into FA and FFA is of great significance in biomass-based transformation. Conventionally, these compounds (FA and FFA) were synthesized using heterogeneous catalysts under high temperature and pressure with O₂/H₂ external sources [8,9]. However, the energy consumption, complexity, and time involved in the classical thermochemical route make the process cumbersome. The complexity of the conventional technique could be eliminated with electrocatalytic conversion reactions, which operate at ambient temperature/pressure, following simple experimental conditions.

Electrocatalysis offers numerous advantages for valorizing biomass-derived feedstocks. The major electrocatalytic reactions involving the oxidation and reduction of feedstock's are compatible with mild acidic and alkaline mediums. The biomass valorization via the electro-oxidation and reduction of the platform FF molecules has been achieved simultaneously at the corresponding anodic and cathodic compartments

* Corresponding author at: Department of Chemistry (BK21 FOUR), Research Institute of Natural Sciences, Gyeongsang National University, Jinju 52828, Republic of Korea.

E-mail address: mychoi@gnu.ac.kr (M.Y. Choi).

¹ These authors contributed equally to this work.

<https://doi.org/10.1016/j.apcatb.2023.123164>

Received 18 April 2023; Received in revised form 13 July 2023; Accepted 10 August 2023

Available online 11 August 2023

0926-3373/© 2023 Elsevier B.V. All rights reserved.

of a typical H-type cell setup. Additionally, the side reactions involved during the reduction and oxidation of FF release H_2 and O_2 gases, which are noninterfering byproducts of the FFA and FA. Considering their functionalities, including $C=C$ at the furan ring and $C=O$ at the side chain, a highly selective reaction of $C=O$ is challenging via oxidation and reduction [10]. Marisa Ketkaew et al. recently reported the simultaneous electrochemical conversion of FF into FFA and FA using a bifunctional Pt/Au Janus electrocatalysts [11]. This approach could relieve the environmental distresses promoted by utilizing petro-fuels and chemicals [12]. Moreover, theoretical studies on metal nanoparticles and structures reveal that the product formation selectivity depends on the furanic compound adsorption site on the metal centers, which relies on the nature of the metals. Thus, FF can be transformed into different products using various catalysts.

Recently, metal–organic framework (MOF)-derived metal oxides successfully retained their structure/morphology and were more chemically stable than MOFs. Generally, MOFs are composed of metal nodes linked to organic ligands, offering more surface area, porosity, and unsaturated metal centers [13,14]. Several studies have prepared metal oxides from MOFs. MOF-derived metal oxides are hollow porous nanostructures with many active sites, and the advantages of designing multi-metal oxides from hetero-metallic MOF structures and C and N-containing ligands acting as nonmetal atom dopants during the calcination of MOF [15]. Additionally, the MOF-derived amorphous carbon framework offers several advantages for electrochemical reactions. Basically, amorphous carbon exhibits a higher surface area due to its structural disorder. The functionalization of heteroatoms (N, O, or S) can improve activity and selectivity. The amorphous nature of the carbon allows high electrical conductivity with rapid electron transfer between the electrode and electrolyte. Furthermore, its excellent chemical stability makes it resistant to degradation and corrosion in alkaline/acidic electrochemical environments, and the low cost of the carbon makes it a promising substrate material for multiple electrochemical reactions [16–19].

Generally, designing a MOF structure involves conventional routes and techniques. Recently, a nonconventional and complex-free pulsed laser ablation in liquid (PLAL) technique has emerged as a novel approach [20–24]. This unique technique offers a one-pot, rapid, non-equilibrium, and byproduct-less materials synthesis [25–28]. Recent literature reflects that the full potential of PLAL has yet to be explored [29–31]. Herein, we synthesized Cu-based MOF via interacting Cu ions with 1,3,5-benzenetricarboxylate (BTC) organic linkers using the PLAL of the Cu target in H_3BTC . Then, the MOF structures were converted into corresponding metal oxides via calcination to deliver higher catalytic activity and structural stability because their catalysts are receiving attention owing to their low cost and high redox tendency. Further, RuO_2 was incorporated to obtain $CuO/RuO_2/C$ nanostructures via a two-step process, i.e., PLAL and calcination, in which low concentrations of noble metal and metal oxides greatly improved the electrochemical oxidation and reduction reactions. Up to now, several Cu-based hybrid materials have been investigated for the efficient conversion of FF into FA and FFA. For instance, Liu et al. investigated the electrochemical hydrogenation (ECH) of FF with various transition metals, including Cu, Pb, Ni, Fe, and Ti. Among them, Cu foil showed the largest shift in the onset potential and resulted in a better current response in the presence of 0.1 M FF, suppressing HER [32]. In another study, Xu et al. developed Cu/NC_{900} and achieved selective ECH of FF into FFA with an FE above 95 % [33]. Similarly, Tian et al. prepared CuO and Ag_2O/CuO for the catalyzed oxidation of furfural into furoic acid, yielding 92 % [34]. Thus, Cu-based electrocatalysts are ideal candidates for the electrocatalytic conversion of aldehydes into their corresponding acids or alcohols. The hydrogen and oxygen evolution, FF hydrogenation, and oxidation reactions (HER, OER, FHR, and FOR, respectively) of these metal oxides were investigated at ambient temperature established on the operating principles of the electrocatalyst in the liquid phase. Moreover, during the electrocatalytic reaction, the molecular

behavior, chemical stability, and selectivity on the surface of the catalyst were monitored using in situ/operando electrochemical (EC)–Raman spectroscopy. This study uncovers the interplay between the potential, oxidation state, and intermediate formation of MOF-derived metal oxides during HER, OER, FHR, and FOR. From the above discussion, we were inspired to develop Cu-based nanostructures with the influence of noble metals to support the electrochemical hydrogenation and oxidation of FF in an alkaline medium.

2. Experimental

2.1. Preparation of Cu-BTC MOF and CuO/C derivative sample

The well-polished Cu plate was placed in a 10 mL of solution containing mixture of DMF and 5 mM concentration of BTC. Then, the Cu plate was ablated via a second harmonic (532 nm) pulsed laser beam with an energy of 80 mJ/cm^2 for 10 min. The obtained pale brown solution was heated overnight at 50°C with a constant stirring at ~ 500 rpm. The blueish-green colloidal solution of Cu-BTC was collected using centrifugation at ~ 14000 rpm. The collected materials were washed twice with ethanol. Then, the obtained colloidal Cu-BTC sample was calcinated at $\sim 350^\circ\text{C}$ for 2 h in the air using a muffle furnace. The calcined samples appeared black. The weight of the as-prepared CuO/C sample after the calcination was 0.2 mg/vial.

2.2. Preparation of $CuO/RuO_2/C$ nanostructures

The $CuO/RuO_2/C$ nanostructures were synthesized using a similar procedure as CuO/C . Herein, 10 mL of 0.4 mM of $RuCl_3$ and 5 mM of BTC in DMF solvent were used for the reaction. Further, the PLAL of the Cu target was performed in the given solution to obtain Cu-BTC MOF along with the co-reduction of Ru ions on the Cu-BTC MOF surface structures. Later, the samples were calcined at $\sim 350^\circ\text{C}$ for 2 h in the air using a muffle furnace to form $CuO/RuO_2/C$ structures on the carbon framework.

The details about the reagents and materials, and characterization techniques are provided in the [Supporting Information](#).

2.3. Electrochemical analysis

The electrochemical performances of the synthesized materials were measured in a 3-electrode H-cell arrangement workstation (CHI 660E), with Hg/HgO and Pt wire as the reference and counter electrodes, correspondingly. The complete electrochemical studies were executed on a carbon cloth (CC) electrode material as the substrate. Herein, commercially procured CC was initially rinsed with a mixture of acetone, ethanol, and water (1:1:1 v/v/v). Later, the CC was immersed in 0.5 M H_2SO_4 for 24 h. Finally, the activated CC was washed with water and ethanol, dried for 10 h under a vacuum, and used as the working electrode for electrochemical reactions. The pretreatment of the CC improves the wettability of the coated electrode in the electrolytic solution. To prepare a uniform catalyst ink, as-prepared CuO/C , and $CuO/RuO_2/C$ samples were thoroughly dispersed in a mixture of Nafion (10 μL), ethanol (45 μL), and water (45 μL) using ultrasonication for 30 min. The resultant ink was drop-coated on the pretreated CC ($1 \text{ cm} \times 1 \text{ cm}$) substrate and dried at ambient temperature. Before the reaction, each compartment of the H-cell was filled with 50 mL of 1.0 M KOH, and N_2 was purged for 30 min. Linear sweep voltammetry profiles were recorded in a 1.0 M KOH medium at 5 mV s^{-1} . The recorded potentials were persuaded into RHE based on the Nernst relation: $E_{RHE} = E_{Hg/HgO} + 0.098 + 0.059 \times \text{pH}$, where the pH of 1.0 M KOH is ~ 14 . The complete overpotential (η) for HER and OER were determined by the formula: $\eta = 0 - E_{RHE}$ V and $\eta = E_{RHE} - 1.23$ V, respectively. The ECSA of all the electrocatalyst samples was evaluated by measuring the electrochemical C_{dl} using CV in the non-Faradaic portion. C_{dl} was calculated using $\Delta j/2 = (j_a - j_c)/2$ vs. the scan rate (mV/s) plot. The slope of the resulting

linear plot represents the C_{dl} of the sample. Similarly, ECSA was determined using the relation: $ECSA = C_{dl}/C_s$, where C_s represents the specific capacitance of the CC (88 mF/cm^2) [13]. The electrochemical impedance spectroscopy (EIS) test was done in a $0.1\text{--}10^5 \text{ Hz}$ with 2 mV amplitude. For the 2 e^- HER and 4 e^- OER processes, TOF (s^{-1}) was calculated by the formula: $TOF (\text{s}^{-1}) = (j \times A)/(2 \times F \times S_a)$ where A , F , and m are electrode surface, the Faradaic constant ($96485.33 \text{ C mol}^{-1}$), and the number of moles of active metal sites, respectively. The available active sites (S_a) were calculated using the equation: $S_a = (j \text{ area of reduction region / scan rate}) / \text{Charge of the electron}$. The mass activity of each catalyst material was calculated using: Mass activity (A g^{-1}) = j/w , where w is the sample weight in g.

2.4. Quantitative analysis of products

The electrochemical conversion of FF into FFA and FA was quantitatively analyzed using an HPLC (YL9100) instrument coupled with an ultraviolet and visible detector (YOUNGIN Chromass). During the electrochemical FHR and FOR, $100 \mu\text{L}$ of the prepared solution was transferred into $3900 \mu\text{L}$ water. During the analysis, the change in the concentration of FFA, FA, and FF was detected at a static wavelength of 216 , 240 , and 276 nm , correspondingly. The column (Agilent SB-C18; $4.6 \times 50 \text{ mm}$, $1.8 \mu\text{m}$, C18) was eluted with a $5 \text{ mM NH}_4\text{HCO}_2$: CH_3OH mixture in the ratio of $95\%:5\%$ at 0.25 mL min^{-1} flow rate in an isocratic mode. Moreover, the yield calculation was based on the calibration curve results obtained for the known concentration of FFA, FA, and FF. The ensuing relations were utilized to determine the conversion of FF into respective products, Faradaic efficiency (FE) based on the charge involved, CB, and selectivity of the desired products (Eqs. 1–3).

$$FE_{\text{FFA or FA}} = \frac{nC_{\text{FFA or FA}} \times F}{Q} \times 100\% \quad (1)$$

$$CB = \frac{C_{\text{FFA or FA}} + C_{\text{FF}}}{C_0} \times 100\% \quad (2)$$

$$\text{Selectivity} = \frac{\text{formed } C_{\text{FFA or FA}} (\text{mol})}{\text{Consumed } FF} \times 100\% \quad (3)$$

Where, C_0 represent the concentration of the FF (50 mM) at the beginning of reactions. n refers the electrons engaged during FOR (2 e^-) and FHR (2 e^-), and Q is the charge utilized during the bulk electrolysis for $\sim 2 \text{ h}$.

2.5. In situ/operando EC–Raman spectroscopy test

In situ/operando EC–Raman probe was studied in a commercially available flow cell setup at redoxme AB, Sweden. The setup was associated to the CHI708E model workstation. The electrochemical flow cell comprised a working electrode (Cu plate connected to ITO substrate), a reference electrode (Ag/AgCl, 3.5 M KCl), and a counter electrode (Pt wire). The catalyst was loaded on the side of an electrically conductive ITO plate. Raman spectra were recorded from 200 to 1000 cm^{-1} using a 532 nm laser attaching $50 \times$ objective lens. The spectrum was recorded in a wide potential range for HER and OER in 0.1 M KOH . Note: in situ/operando electrochemical studies were achieved by an Ag/AgCl electrode, while the common electrochemical reactions were studied by Hg/HgO electrode.

3. Results and discussion

3.1. Material formation and mechanism

Cu-BTC is known as HKUST-1, a well-studied MOF for heterogeneous catalysis, energy, and gas storage applications. A paddle wheel complex of the 3-dimensional hierarchical structure of Cu-BTC is made from the interaction of Cu^{2+} ions and 1,3,5-benzene tricarboxylate linkers [35].

The formation dynamics of the Cu-BTC were as follows: $2 \text{ BTC}^{3-} + 3 \text{ Cu}^{2+} \rightarrow \text{Cu}_3(\text{BTC})_2$. During the MOF synthesis, we could achieve $\text{Cu}_3(\text{BTC})_2$ with a more pore volume and surface area [36]. Despite having structural advantages, these MOF structures limit their conductivity and chemical stability for long repetitive cycles. To overcome these shortcomings, we employed Cu-BTC MOF as a template or substrate to build a metal oxide with a designated structure, homogeneous distribution, and porosity, providing robust electrocatalytic and electrochemical properties [37]. A detailed explanation for the formation mechanism of Cu-BTC and similar MOFs using PLAL has been presented in our previous study [13]. In our investigation, the octahedral Cu-BTC has retained its morphology after heating at 350°C for 2 h , resulting in pristine CuO/C on the carbon framework. The sacrificial MOF acts as a substrate for nanosized CuO and allows other dopants to deposit on the surface to form a heterojunctions [38]. Bimetallic oxide nanostructure is an advanced method to improve the electrochemical accomplishment of the material toward energy conversion reactions. On that note, Cu-BTC MOF material was synthesized under a Ru^{3+} salt solution. During the ablation of the Cu target using a second harmonic laser, Ru^{3+} ions undergo photoreduction and deposit on the Cu-BTC MOF structure. Because Cu-BTC being moderate chemical stability, Cu-BTC/Ru was calcined again at 350°C for 2 h to achieve CuO/RuO₂/C. The optimum calcination temperature was chosen to completely oxidize both elements to form composite structures [39].

Fig. 1a displays a schematic representation of Cu-BTC, CuO/C, and CuO/RuO₂/C nanostructure synthesis using unique PLAL. The morphology and elemental composition of the synthesized Cu-BTC, CuO/C, and CuO/RuO₂/C nanostructures were examined by FE-SEM and HR-TEM analyses. The laser-synthesized Cu-BTC has an octahedral shape, which is well preserved after calcination to form CuO at the carbon framework, as shown in Fig. 1. The FESEM images of the homogeneous submicron size Cu-BTC MOF, CuO/C, Cu-BTC/Ru, and CuO/RuO₂/C structures and their EDS mapping images are shown in Fig. S1. HR-TEM also clearly depicts the octahedral shape of the carbon framework, which is retained after the calcination of the Cu-BTC MOF structure, as revealed in Fig. 1b. Additionally, Fig. 1(b-i) shows pores that evolved during the open-air calcination of the MOF materials. These porous C structures can facilitate and improve the electron transfer properties of the electrochemical reactions. The selected area region of the HR-TEM images was given in Fig. 1(c-i), which corresponds to a digital diffraction pattern obtained through the Fast Fourier transform (FFT) technique. This diffractogram shows sharp crystalline spots corresponding to CuO and RuO₂ in the composite, which can be indexed to the characteristic monoclinic phase of CuO with the (002) plane [40]. The calculated d-spacing for the selected spots in the FFT analysis corresponds to a distance of 0.25 nm , which is consistent with the (002) lattice of polycrystalline CuO (Fig. 1(b-i)) [41]. Similarly, we could observe the presence of RuO₂ on the CuO/C nanostructure with 0.227 nm d-spacing for the RuO₂ (200) plane, as shown in Fig. 1(c-c(i)) [42].

Interestingly, the uniformly distributed RuO₂ did not affect the native octahedral structure of Cu-BTC. Further, STEM-EDS investigation approves the existence of Cu, O, Ru, and C species in the CuO/RuO₂/C nanostructure, as shown in Fig. 1(d-d(iv)). The EDS mapping show that the elemental composition in the final CuO/RuO₂/C is Cu = 18.95 wt\% , O = 25.23 wt\% , C = 52.18 wt\% , and Ru = 3.64 wt\% , which reveals the synthesized nanostructures with a low Ru percentage to investigate its effect on electrocatalytic oxidation and reduction. Additionally, the calculated average size distribution of CuO and RuO₂ was $\sim 9.21 \pm 0.25$ and $16.61 \pm 0.7 \text{ nm}$, respectively, as depicted in Fig. S2.

The synthesized Cu-BTC, CuO/C, and CuO/RuO₂/C were further analyzed using XRD. The obtained Cu-BTC MOF structures are identical and compiled with the HKUST-1 MOF structure (CCDC No.112954) (Fig. S3) [13,43]. The as-prepared CuO/C nanostructures exhibit a monoclinic structure with high crystallinity and phase purity, as revealed in Fig. 2a. The recorded XRD spectral peaks at 32.5° , 35.5° ,

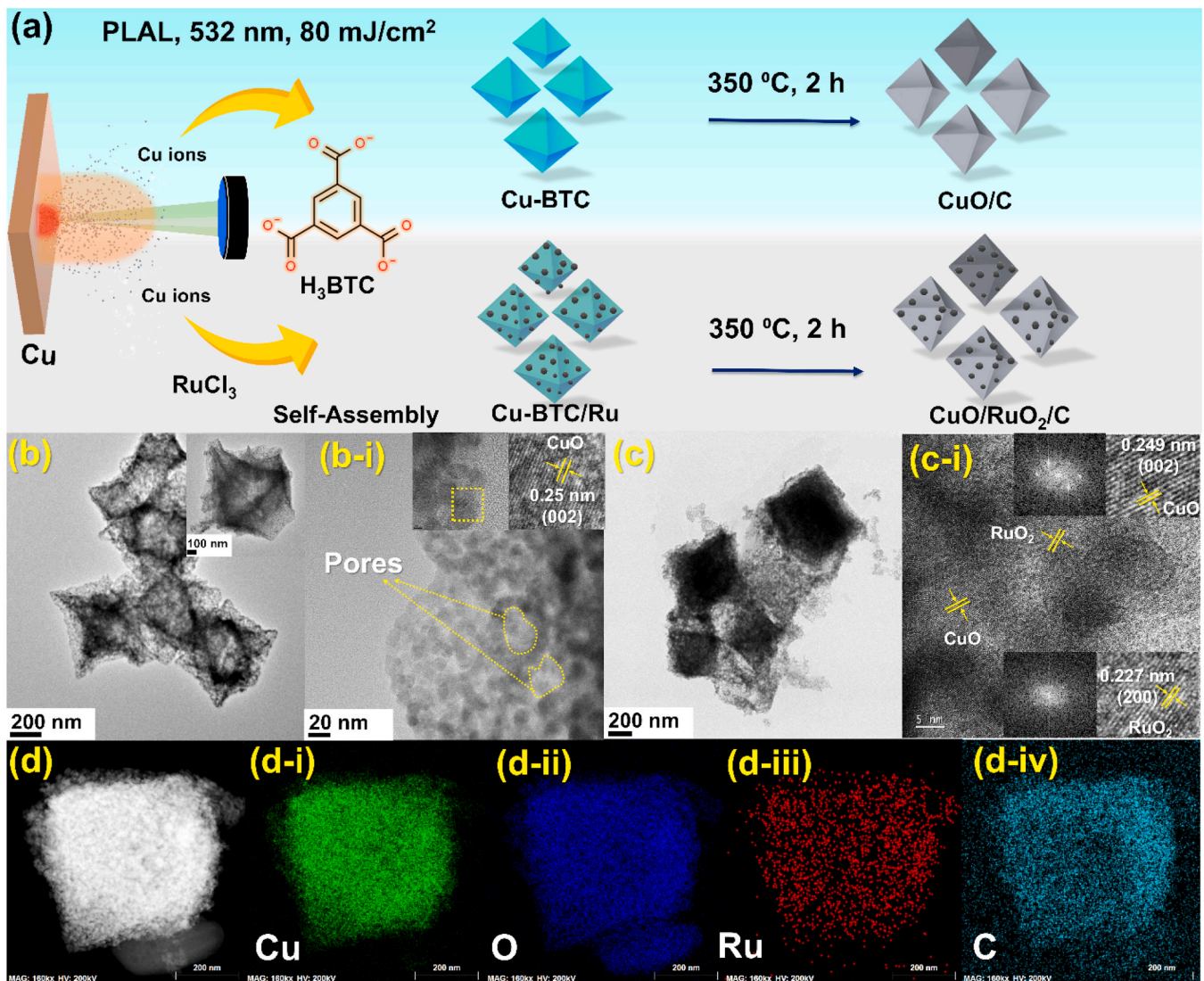


Fig. 1. (a) The schematic depiction of the MOF-derived CuO/C and CuO/RuO₂/C nanostructure using the pulsed laser technique. (b & b-i, c & c-i) TEM and HR-TEM pictures of the CuO/C (b and b-i) and CuO/RuO₂/C (c and c-i) nanostructures. (d and d-i-iv) elemental analysis of CuO/RuO₂/C nanostructure with scanning transmission electron microscopy (STEM) coupled with EDS.

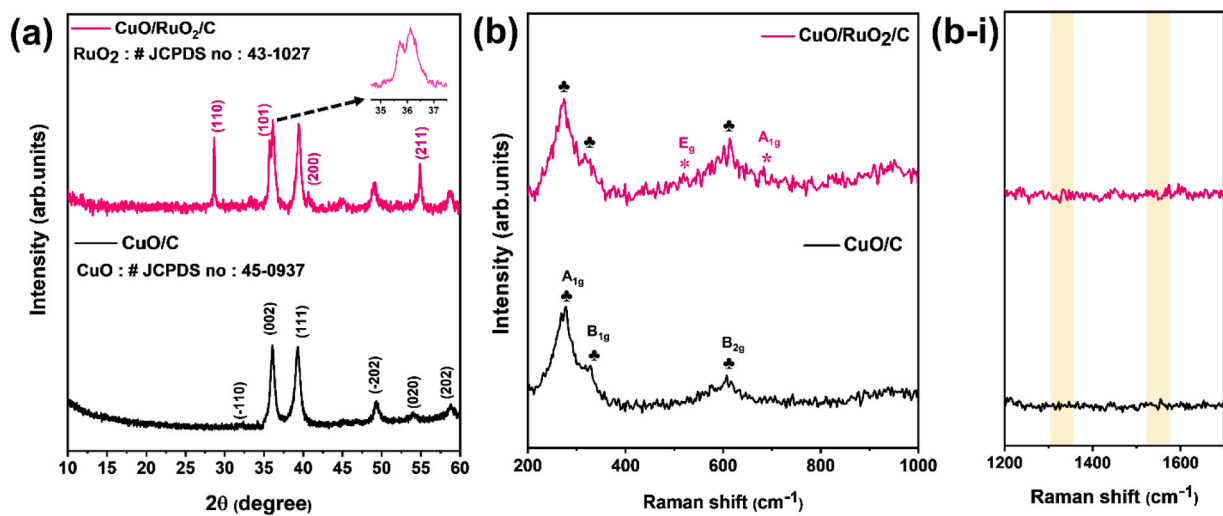


Fig. 2. (a) XRD and (b and b-i) Raman spectra of CuO/C and CuO/RuO₂/C.

38.8°, and 48.9°, respectively, corresponding to the (−110), (002), (111), and (−202) planes of a typical single tenorite phase structure of CuO/C (JCPDS card no. 00–045–0937) [41,44]. The monoclinic phase structure of CuO has an axial translation $a \neq b \neq c$ along with a lattice constant $\alpha = \gamma = 90^\circ$ and $\beta > 90^\circ$ [45]. Furthermore, the XRD spectrum of CuO/RuO₂/C reveals prominent peaks corresponding to CuO, along with additional new peaks at 28.6°, 36.1°, 40.7°, and 54.8°, which can be attributed to the (110), (101), (200), and (211) planes of tetragonal RuO₂, as shown in Fig. 2a (JCPDS No #040–1290) [46]. Thus, the results confirm a fine formation of CuO/RuO₂/C nanocomposites without any other impurities.

We performed Raman spectroscopic analysis to understand the vibration modes in the CuO/C and CuO/RuO₂/C nanostructures. Raman spectroscopy is known for its versatility in the real-time measurement of change in the oxidation state, intermediate molecular state, bond vibrations, amorphous, and recrystallization of the catalyst during redox reactions. The CuO/C is C_{2h} space group with two molecules/primitive cell. Hence, the zone center Raman modes of CuO are $\Gamma_{\text{RA}} = 4A_u + 5B_u + A_g + 2B_g$, in which there are three acoustic modes ($A_u + 2B_u$), six IR modes ($3A_u + 3B_g$), and three Raman modes ($A_g + 2B_g$). As shown in Fig. 2b, three prominent Raman peaks of CuO/C are A_{1g} (272 cm^{−1}), B_{1g} (321 cm^{−1}), and B_{2g} (612 cm^{−1}) [47,48]. Thus, the Raman bands corresponding to the CuO are visible in CuO/C and CuO/RuO₂/C. Surprisingly, the absence of distinctive characteristic peaks of carbon in XRD and Raman analyses can be attributed to the presence of amorphous or a low degree of graphitization in the structure, Fig. 2(b–i) [49, 50].

In addition to the bands of CuO, low-intensity RuO₂ vibrational modes were observed at 522 and 682 cm^{−1}, representing E_g and B_{2g} modes, respectively. Hence, crystal structure and vibrational characteristics confirm the formation of the CuO/RuO₂/C [51,52].

XPS was employed to further examine the composition, binding energies, and oxidation states of the CuO/C and CuO/RuO₂/C. Fig. 3a displays the survey of CuO/C and CuO/RuO₂/C recorded with Cu 2p, O 1s, C 1s, and Ru 3p spectra. Initially, the spectrum was adjusted for the standard C 1s spectra positioned at 284.6 eV. The high-intensity C 1s peak was present at 284.6 eV, corresponding to the sp² C=C peaks of the MOF structure (Fig. 3b). When the C 1s peak was deconvoluted, the resolved low-intensity peaks were associated with the sp³-hybridized C-C observed at 285.9 eV. The same C 1s chemical composition was observed even in CuO/RuO₂/C [53,54]. The analyzed results in Fig. 3a show high-intensity peaks corresponding to the Cu 2p, C 1s, and O 1s states. As depicted in Fig. 3c, Cu 2p exhibits two main peaks at the BE of

934.25 and 954.25 eV, corresponding to the spin-orbital coupling of Cu 2p_{3/2} and Cu 2p_{1/2} with a BE difference (ΔBE) of 20 eV, indicating the +2 state of Cu [55–57]. Thus, MOF-derived Cu_xO is completely oxidized to form Cu(II)O [56]. Moreover, CuO exhibited the characteristic satellite peaks of the resulting unfilled Cu 3d⁹ shell in the CuO (Fig. 3c) [58]. The anionic part of CuO, i.e., O 1s XPS spectra, revealed a large peak located at 529.77 eV, as depicted in Fig. 3d. The asymmetric peak of the O 1s deconvoluted spectra exhibited three additional components at approximately 529.66, 531.29, and 532.96 eV. These components were attributed to lattice oxygen (Cu–O), chemisorbed/dissociated oxygen species (O^{2−}, O₂[−], or O[−]), and C=O/C–O states, respectively [59–63]. Similarly, CuO/RuO₂/C shows C 1s, Cu 2p, O 1s, and Ru 3p (Fig. 3e–h). The occurrence of Cu in the +2 state, even in the CuO/RuO₂/C composite, reveals the formation of single-phase CuO (Fig. 3f). The CuO/RuO₂/C composites O 1s spectra appear at a BE of 529.4 eV, as shown in Fig. 3g. Deconvolution of the O 1s spectra reveals additional peaks at 529.40, 531.2, and 532.9 eV, assigned to the oxygen lattice between M–O, chemisorbed oxygen in the composite, and C=O or C–O, respectively. High-resolution XPS shows major doublets at 462.64 and 484.93 eV for the spin-orbital coupling of Ru 3p_{3/2} and Ru 3p_{1/2} in RuO₂. The deconvolution of the spectra exposed that 462.64 and 484.93 eV can be deconvoluted, which were assigned for Ru 3p_{3/2} and Ru 3p_{1/2} representing the Ru⁴⁺ valence state in RuO₂. Additionally, a low-intensity shoulder peak appeared at 465.59 and 487.60 eV, depicting the satellite peaks of Ru 3p_{3/2} and Ru 3p_{1/2} spin-orbital coupling of RuO₂ (Fig. 3h) [64].

3.2. Electrocatalytic HER and FHR analyses

After the systematic characterization, the developed CuO/C and CuO/RuO₂/C catalysts were converted into a catalyst ink and well-coated on CC as the working electrode for the electrochemical reactions. The complete reactions were investigated in an H-cell at ambient temperature. Initially, a CV test was performed to activate the electrocatalyst at 50 mV s^{−1} in 1.0 M KOH until the anodic and cathodic peak current attained a saturation point. Fig. 4a shows the LSV cathodic polarization curve obtained for Pt/C, CuO/C, and CuO/RuO₂/C at 5 mV s^{−1} in the 0 to −0.6 V vs. RHE. Pt/C was used as a catalytic benchmark for the performance comparison study. From the LSV curve shown in Fig. 4b, the overpotential (η_{10}) obtained for Pt/C, CuO/C, and CuO/RuO₂/C were 55, 384, and 127 mV, respectively. This indicates that RuO₂ in the CuO/RuO₂/C interface structure boosts the HER performance by lowering the overpotential in the alkaline medium. To

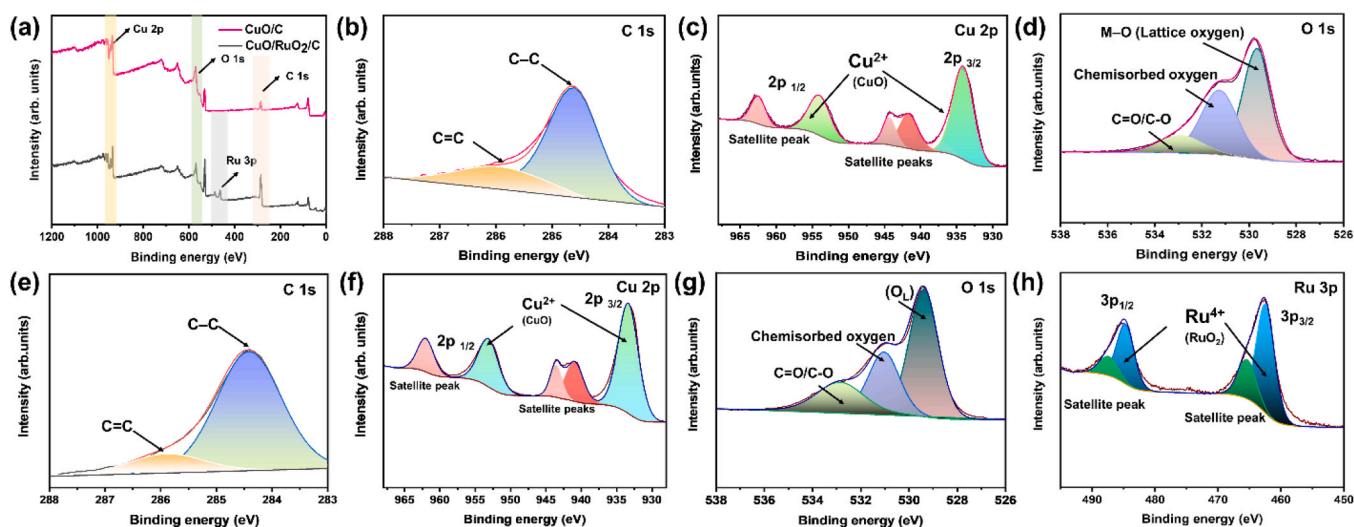


Fig. 3. (a) XPS survey of CuO/C and CuO/RuO₂/C. (b, c, and d) High-resolution XPS of C 1s, Cu 2p, and O 1s of CuO/C. (e–h) Core-level XPS of C 1s, Cu 2p, O 1s, and Ru 3p of CuO/RuO₂/C, respectively.

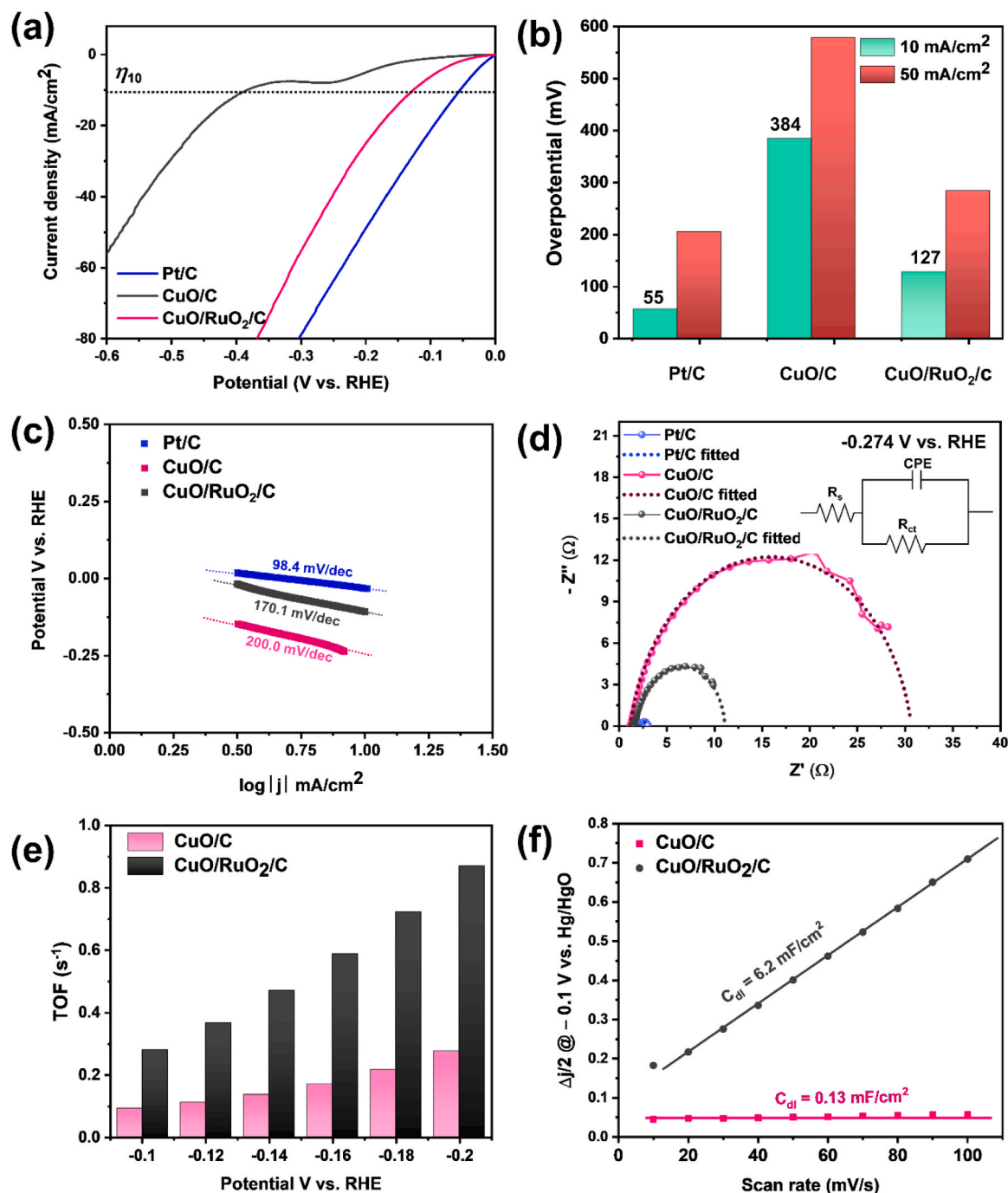


Fig. 4. (a) Cathodic polarization curve during HER, (b) comparative HER of Pt/C, CuO/C, and CuO/RuO₂/C at 10 and 50 mA cm⁻², (c) Tafel plot, (d) EIS Nyquist graph of the electrocatalyst at -0.274 V vs. RHE with a fitted Randles circuit, (e) TOF of the electrocatalyst in -0.1 to -0.2 V vs. RHE, and (f) C_{dl} graph obtained from the CV curve of the non-Faradaic region.

illustrate the reaction kinetics and mechanism of the electrocatalyst during HER, Tafel slopes are transformed and fitted according to the Tafel equation based on the cathodic LSV profile. From Fig. 4c, Pt/C has the lowest Tafel slope of 98.4 mV dec⁻¹, which can be considered a state-of-the-art catalyst for HER. In contrast, CuO/C and CuO/RuO₂/C exhibit Tafel slope values of 200.0 and 170.1 mV dec⁻¹, correspondingly. The smallest Tafel slope of CuO/RuO₂/C reveals the fast reaction kinetics of the CuO/RuO₂ interface during HER. During HER, H₂ evolution could occur via three major steps in an alkaline medium: (i) Volmer step (120 mV dec⁻¹) $\ast + e^- + H_3O^+ \rightarrow \ast H_{ads} + H_2O$; (ii) Heyrovsky step (40 mV dec⁻¹) $\ast H_{ads} + H_3O^+ + e^-$; (iii) Tafel step (30 mV dec⁻¹) $\ast H_{ads} + \ast H_{ads} \rightarrow 2\ast + H_2$. Herein, “ \ast ” signifies the active metal

site. According to the equation, the best-performing CuO/RuO₂/C nanostructure follows the 2e⁻ Volmer–Heyrovsky steps, with the Volmer step being the RDS of the reaction. Further, EIS validates the electron transfer ability and kinetics of the designed electrocatalysts. The smaller the semicircle radius in the EIS Nyquist graph, the better the electron mobility. Owing to the apparent role of the catalyst in transferring the charges to dissociate water molecules to generate hydrogen molecules, the charge transfer resistance (R_{ct}) is considered a crucial factor for determining HER [65]. To understand R_{ct} , the Nyquist plots were recorded at a constant potential of -0.274 V vs. RHE. This plot provides a relationship between the real and negative imaginary components. Additionally, an equivalent circuit model was used to correlate the

modulation in the Nyquist plot with respect to change in the charge transfer property of the electrode material. The obtained Nyquist plots were fitted, and the corresponding equivalent Randles circuit was achieved using Z-view software. The equivalent circuit consists of capacitance and phase elements (CPE), series resistance (R_s), and charge transfer resistance (R_{ct}). The fitted graph matches well with the experimentally obtained results, as denoted by the dotted curve. Fig. 4d shows the generated equivalent circuit from which the R_{ct} was calculated. Further, Fig. 4d displays that Pt/C shows the smallest semicircle with an R_{ct} of 0.93 Ω , followed by CuO/RuO₂/C (5.2 Ω) and CuO/C (29.5 Ω). This manifests that the fastest interfacial charge transfer kinetics were expected in CuO/RuO₂/C nanostructures than that of bare CuO/C. The intrinsic activity of the designed CuO/C and CuO/RuO₂/C nanostructures were illustrated using TOF and mass activity. Fig. 4e presents

the overall H₂ turnover per second from the available active sites of the electrocatalyst. At the linear potential (−0.1 to −0.2 V vs. RHE) region, the TOF was higher for CuO/RuO₂/C than that for CuO/C. For instance, the TOF of CuO/C and CuO/RuO₂/C were 0.276 and 0.870 s^{−1}, respectively at −0.2 V vs. RHE. This indicates that the available RuO₂ provides higher active sites for promoting H₂ evolution. To deeply understand the HER kinetics, we calculated mass activity at the linear cathodic potential of CuO/C and CuO/RuO₂/C. Thus, the results of mass activity measurements also endorse the enhanced HER activity of CuO/RuO₂/C than that of CuO/C, as shown in Fig. S4. Further, ECSA reveals the essential number of exposed active sites for oxidation–reduction over the electrocatalyst, which can be estimated from C_{dl} by plotting the scan rate versus the average difference between cathodic and anodic current densities. The C_{dl} slope values for CuO/C and

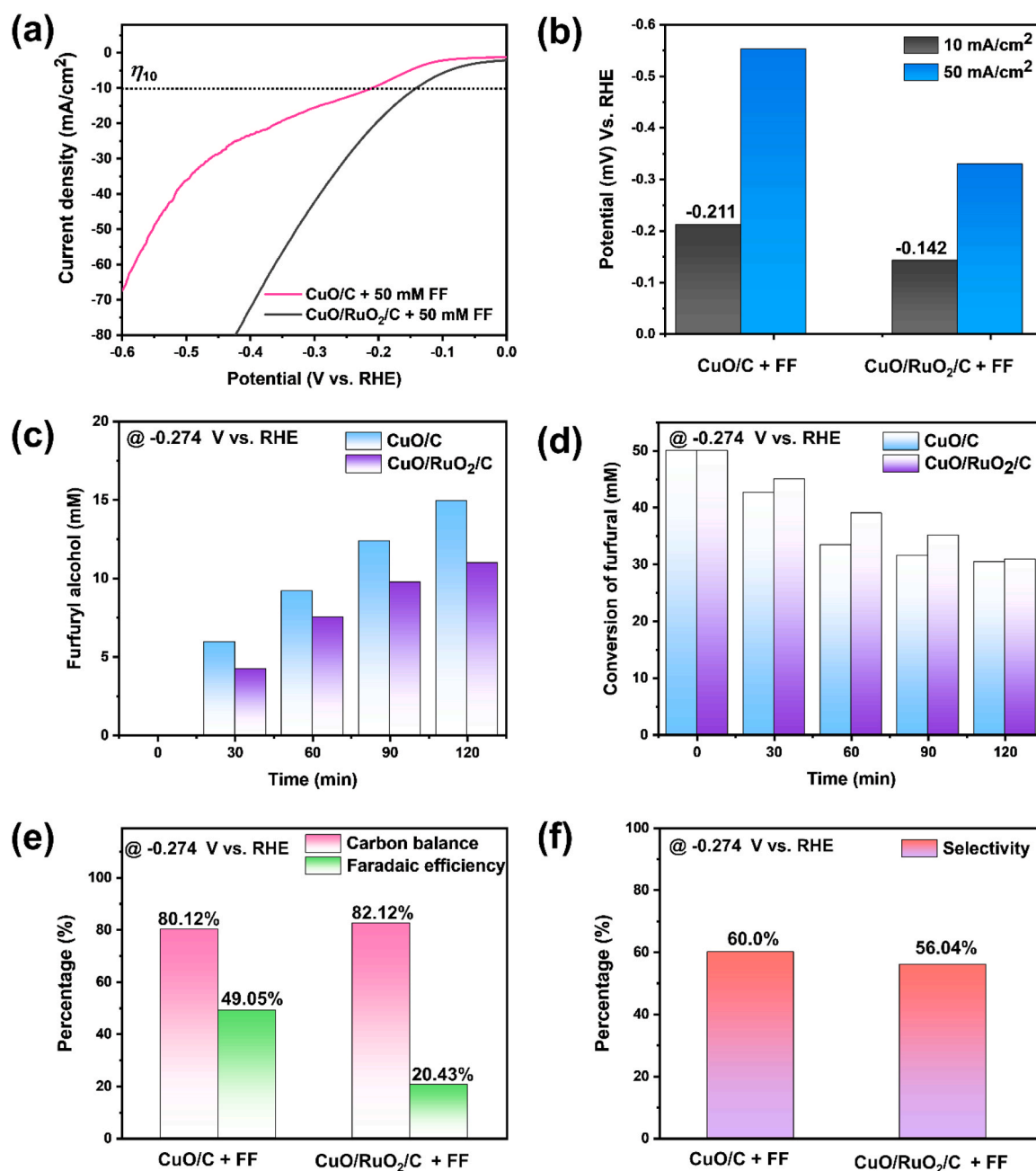


Fig. 5. (a) LSV curve of CuO/C and CuO/RuO₂/C with 50 mM FF, (b) comparative potential graph to realize 10 and 50 mA cm^{−2} in the presence of 50 mM FF, (c) furfuryl alcohol formation using CuO/C and CuO/RuO₂/C at −0.274 V vs. RHE, (d) conversion of FF during FHR at −0.274 V vs. RHE for 120 min, (e) calculated CB and FE for CuO/C and CuO/RuO₂/C at −0.274 V vs. RHE, and (f) selectivity of electrocatalyst for the FFA formation.

CuO/RuO₂/C are 0.13 and 6.2 mF cm⁻² (Figs. S5 and 4f), respectively, and the obtained C_{dl} of the samples are thereby theoretically proportionate to ECSA. Fig. 4f shows that introducing a low amount of RuO₂ can manifest and increase ECSA and expose higher active sites, resulting in better catalytic action than that of the bare CuO/C catalyst (Table S1). The performance of the synthesized electrocatalysts toward HER was compared with the previously reported materials and tabulated in Table S2. Finally, FE-SEM and EDS images, as well as XRD analysis, were utilized to determine the structural stability of the CuO/RuO₂/C sample. From Fig. S6 and S7, it is evident that the CuO/RuO₂/C sample remains structurally and chemically stable after the HER process.

Considering the optimized performance of CuO/C and CuO/RuO₂/C during HER, we employed FHR under the same experimental condition as that of HER using a 50 mM FF in a 1.0 M KOH. A complete pictorial representation of the H-cell setup is specified in Fig. S8. As exposed in Fig. 5a, the LSV of CuO/C and CuO/RuO₂/C was performed under the cathodic potential in the presence of FF. During LSV at the cathodic potential, the performance of the CuO/C was increased by lowering the potential. In contrast, CuO/RuO₂/C did not considerably improve their activity toward FHR because FF reduction is more prone to occur in CuO/C than in CuO/RuO₂/C, which is highly effective toward the counterpart HER. As revealed in Fig. 5b, a 10 and 50 mA cm⁻² was attained at the potential of -0.211 and -0.533 mV for CuO/C and -0.142 and -0.328 mV for CuO/RuO₂/C electrocatalyst, respectively. To further investigate the electrocatalytic hydrogenation of FF, we performed bulk electrolysis (time versus current at constant potential). Initially, the efficiency of CuO/C and CuO/RuO₂/C was measured at -0.274 V vs. RHE. The response current-time curve was recorded for 120 min, and the resultant catholyte was measured every 30 min using HPLC. Fig. 5c shows that the conversion of FF into FFA was started at the beginning. Moreover, the FFA concentration gradually increased as the charge passed for 120 min. The conversion of FF into FFA was more effective for the CuO/C electrocatalyst (14.93 mM) than that for the CuO/RuO₂/C (10.98 mM) electrocatalyst (Fig. 5c). Moreover, we studied the effect of applied cathodic potential for converting FF into FFA on CuO/C. The conversion of FF into FFA at -0.174 (12.5 mM), -0.274 (14.93 mM), and -0.374 (12.9 mM) V vs. RHE is presented in Fig. S9. Similarly, the changes in the FF concentration were also monitored during the electrochemical reaction via HPLC, as shown in Fig. 5d. The starting FF was consumed during the electrochemical FHR, the remaining FF concentration after 120 min were 30.41 and 38.86 mM for CuO/C and CuO/RuO₂/C electrocatalysts, respectively.

The recorded HPLC spectra of CuO/C and CuO/RuO₂/C during continuous FHR for 120 min at -0.274 V vs. RHE are given in Fig. S10. Moreover, we have also provided actual image results of CuO/C sample during FHR, as recorded through HPLC in, Fig. S11. The FHR kinetics over CuO/C and CuO/RuO₂/C could be illustrated based on CB (%), FE (%), and selectivity (%). Fig. 5e depicts the highest FE value of 49.05 % for CuO/C, overpassing the lowest FE of 20.43 % for CuO/RuO₂/C. This indicates that CuO/C was utilized for the selective conversion of FF by suppressing HER or any other side reactions at the optimal applied potential. However, CuO/RuO₂/C is more susceptible to HER than FHR under the applied potential. The calculated CB for CuO/C and CuO/RuO₂/C is 80.12 % and 82.12 %, respectively. The best-performing CuO/C showed the highest selectivity of 60.0 % compared to CuO/RuO₂/C (56.04 %), and the above results were justified by the FE of the samples, as shown in Fig. 5f.

Additionally, it is important to elucidate the active site, selectivity, and the relevant reaction mechanism involved during the FHR, which are crucial to developing hybrid electrocatalysts. Fig. 6 shows that CuO/C improved FHR activity by lowering the reaction potential with 50 mM FF. In contrast, CuO/RuO₂/C did not show an evident change in the FHR activity like the HER performance. The CuO/RuO₂/C activity decreased in the presence of FF, contrary to the hypothesis of lowering the potential of the electrocatalyst in the presence of FF. The primary reason for this tendency is the forbidden interaction of FF with Cu active site owing to the existence of RuO₂ structure. During FHR, the fully oxidized CuO in the +2 oxidation state undergoes a phase transformation from Cu²⁺ to Cu⁺ oxidation state under the negative potential (-0.1 to -0.5 V vs. RHE); $2\text{CuO} + \text{H}_2\text{O} + 2\text{e}^- \rightarrow \text{Cu}_2\text{O} + 2\text{OH}^-$ [66]. Pang et al. proposed that the low valence Cu oxidation state could be a major active site for reducing organic molecules [66]. Rao et al. stated that the TOF of the CuCrO₂ was dependent on the number of Cu⁺ active sites [67]. Nonetheless, identifying the active sites in the Cu-based catalysts has been debated. However, the experimental results and DFT calculations provided sufficient evidence to predict the active site and reaction dynamics. Xing-Xing et al. state that during electrochemical reduction or oxidation, Cu_xO could transform into Cu₂O and CuO, which is an active site for HER and OER, respectively [68]. The XRD analysis was performed before and after the FHR in 1.0 M KOH to confirm the active site of CuO. The changes in the partial surface structural reorientation can be explained through the changes in the oxidation state of CuO/C. Thus, the surface composition and oxidation state of CuO/C were studied before and after the FHR using core-level XPS analysis.

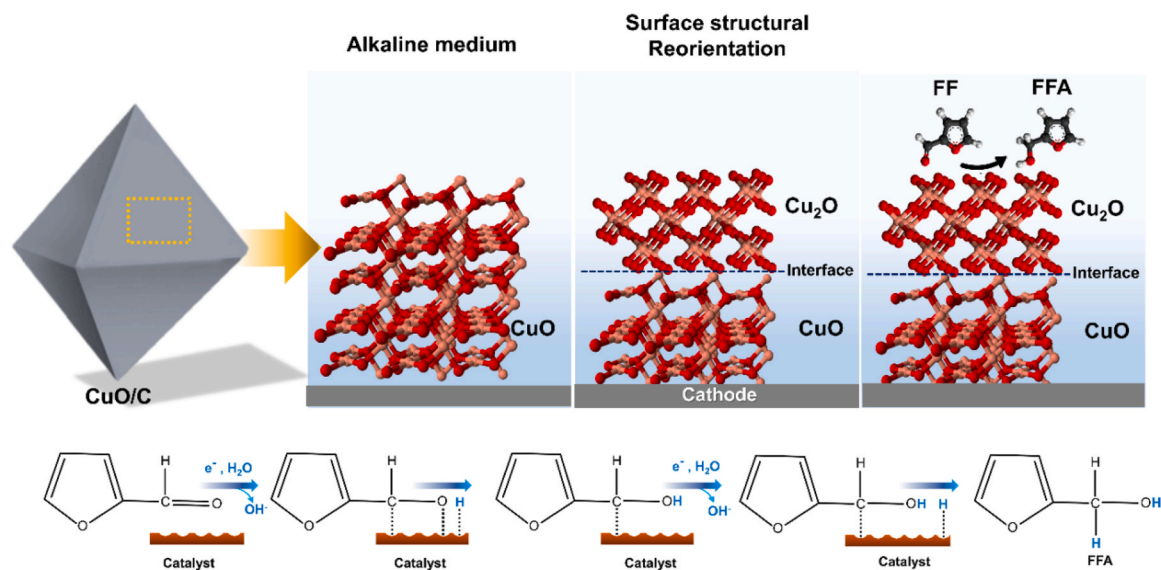


Fig. 6. The schematic illustration of the catalyst behavior mechanism during FHR in 1.0 M KOH medium, the interaction mechanism of FF, and the active sites for converting FF into FFA.

Fig. S12 presents the XPS spectra of Cu 2p for CuO before and after FHR. Before the FHR, the Cu 2p orbital of CuO exhibits high-intensity doublet peaks at ~ 934.20 and 954.21 eV, corresponding to the Cu $2p_{3/2}$ and $2p_{1/2}$ spin-orbital splitting of CuO. This indicates that Cu in the CuO structure has only a +2 oxidation state [69]. The same CuO/C sample was analyzed after the FHR of 120 min using XPS. Surprisingly, after the reaction, the XPS spectrum for the Cu 2p orbital of CuO records additional well-resolved peaks with low BE ~ 932.39 and 952.31 eV representing the Cu $2p_{3/2}$ and $2p_{1/2}$ of the Cu^+ oxidation state, confirming the presence of Cu_2O in the structure. In addition, we could observe a deconvoluted peaks at 934.57 and 954.60 eV for the Cu^{2+} oxidation state [70]. The small shift in the positive BE is owing to the

interfacial charge transfer between the CuO and Cu_2O electronic structure. Hence, CuO/C sample was transformed and exhibited a dual-phase structure during FHR. However, the same sample could transform and retain its initial CuO/C state after performing other (oxidation) half-reactions. Cu-based electrocatalysts show the highest selectivity to deliver FFA as a major product. The conversion of FF into FFA on a Cu-based electrocatalyst was as follows: during the electrocatalytic FHR, the carbonyl group of FF showed the highest tendency to interact with the catalyst via the $\eta^1(\text{O})$ -aldehyde conformation because the interaction of catalyst site with $\text{C}=\text{C}$ of furan ring is weak [71]. The terminal O atom of FF is adsorbed on the O vacancies of the electrocatalyst surface (Cu_2O), forming a chemical bond between FF and Cu_2O active sites.

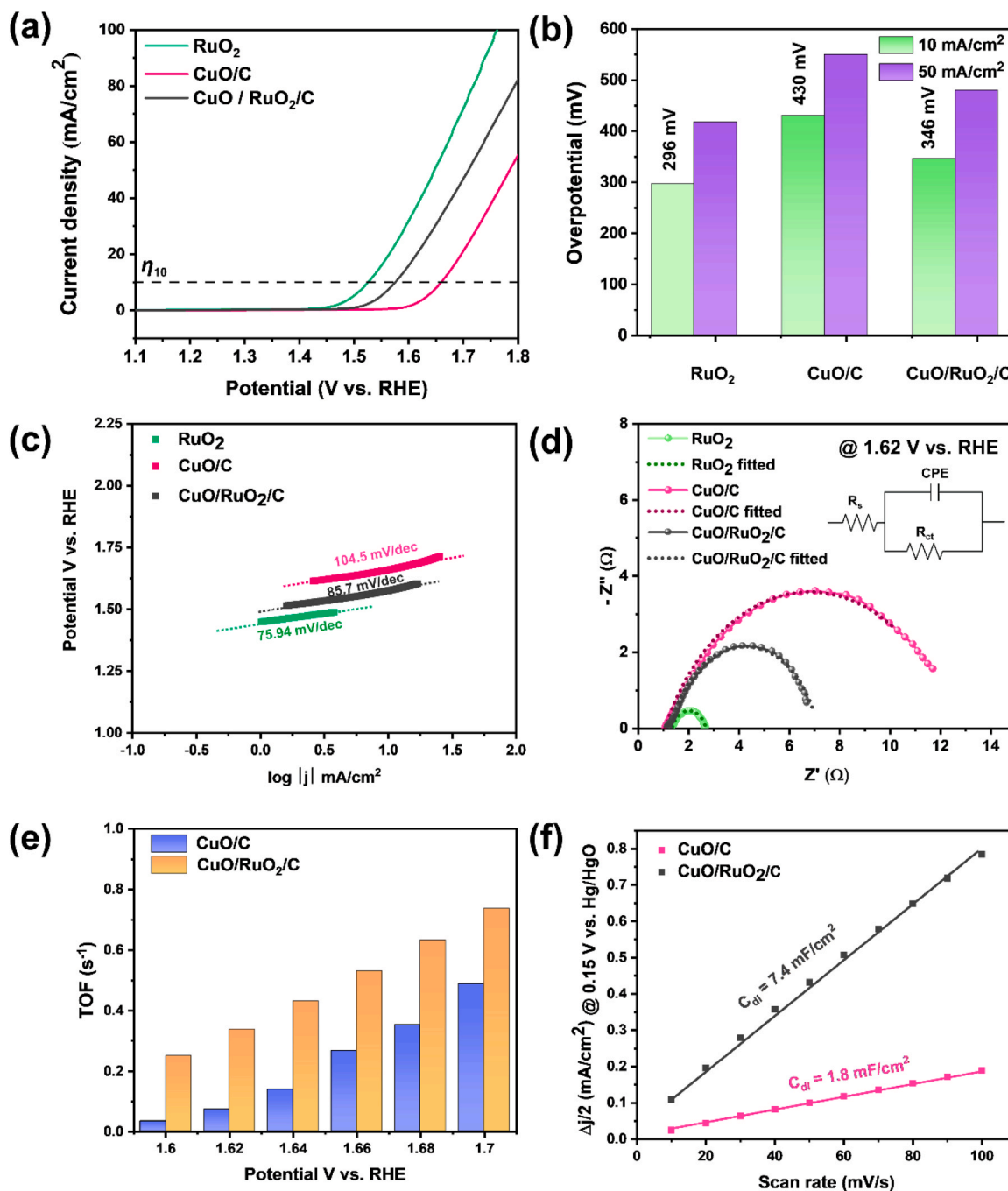


Fig. 7. (a) LSV curves measured in the anodic potential during OERs, (b) the overpotential graph of the electrocatalyst to attain 10 and 50 mA cm^{-2} , (c) the Tafel plot of RuO_2 , CuO/C , and $\text{CuO}/\text{RuO}_2/\text{C}$ for reaction kinetic studies, (d) the Nyquist graph of the catalysts at 1.62 V vs. RHE and corresponding equivalent circuit, (e) TOF graph, and (f) C_{dl} graph of CuO/C and $\text{CuO}/\text{RuO}_2/\text{C}$ electrocatalysts.

Further, under a proton-coupled electron transfer reaction, the chemically bonded FF molecule converted into FFA, as exposed in Fig. 6. Importantly, the H^+ adsorption is a crucial step, which can be achieved via the Volmer reaction [72].

3.3. Electrocatalytic OER and FOR analyses

The electrocatalytic activity of the synthesized sample was examined toward OER and FOR in a 1.0 M KOH. Initially, the OER performance was studied without 50 mM FF in the H-type cell compartment. First, electrode materials were activated by performing CV analysis in the anodic region by applying positive potentials. The CV curves were recorded until the curve reached a saturated current density. The OER of CuO/C, CuO/RuO₂/C, and commercial RuO₂ (for comparison) was assessed using the LSV curves [73]. Interestingly, all the synthesized electrocatalysts exhibited significant performance toward OER, as depicted in Fig. 7a. To understand the material activity, overpotential (η_{10}) was examined, as shown in Fig. 7b, in which commercial RuO₂ (η_{10} = 296 mV) demonstrated the lowest overpotential, whereas low wt% RuO₂-modified CuO/C (η_{10} = 346 mV) nanostructure exhibits apparent improvement when compared to CuO/C (η_{10} = 430 mV). The OER activity of CuO/RuO₂/C is superior to the recent literature reports (Table S3). Thus, the improved activity of the electrocatalyst might be influenced by the O vacancies and electronic coupling between the CuO and RuO₂ nanostructures. The O vacancies can occur during the calcination of Cu-BTC, where the Cu-BTC structure tends to undergo changes in the oxidation state at elevated temperatures. This results in the formation of Cu₂O or Cu⁰ as an intermediate product. Further, the Cu₂O or Cu⁰ can react with the oxygen in the surrounding atmosphere to form a CuO structure. This process may induce O vacancies within the CuO lattice, also referred to as oxygen defect states. These O vacancies in the optimal CuO/RuO₂/C catalyst can enhance OER performance by providing additional active sites on the material's surface. Interestingly, O vacancies can lower the energy barrier for OER by facilitating the dissociation of water molecules and the formation of oxygen intermediates. Additionally, O vacancies modify the electronic structure of CuO and RuO₂, which can weaken the O-H bonds in water molecules and promote the release of O₂ [74].

Furthermore, the corresponding Tafel slope derived from the polarization curve is considerably smaller for CuO/RuO₂/C (85.7 mV dec⁻¹) than that for CuO/C (104.5 mV dec⁻¹), indicating that the presence of RuO₂ impressively accelerated the OER kinetics (Fig. 7c). The stepwise mechanism involved in the O₂ evolution was previously studied [29,75]. The EIS results of CuO/C, CuO/RuO₂/C, and commercial RuO₂ agree with the LSV results. The R_{ct} kinetics of the electrode materials were measured using EIS at 1.62 V vs. RHE. Here, the fitting curves (represented as dotted lines) for each sample match well with the experimental results (represented by symbol with curved lines), demonstrating that the chosen equivalent circuit model is highly viable (Fig. 7d). Among the as-prepared electrocatalysts, the fitted curve for CuO/RuO₂/C has a small diameter semicircle and exhibits the smallest R_{ct} . Fig. 7d shows the recorded R_{ct} for RuO₂, CuO/C, and CuO/RuO₂/C, which are 1.35, 11.5, and 5.84 Ω , respectively. The intrinsic activity of the CuO/C and CuO/RuO₂/C materials was measured using TOF calculations. Fig. S13 depicts more available active sites for CuO/RuO₂/C than that for CuO/C to generate O₂. Thus, we could observe the highest O₂ evolution rate for CuO/RuO₂/C in the linear potential range of 1.6–1.7 V vs. RHE (Fig. 7e), and the calculated TOF for CuO/C and CuO/RuO₂/C are 0.48 and 0.73 s⁻¹ respectively, at 1.7 V vs. RHE. Another parameter to elucidate the intrinsic activity is mass activity performance. CuO/RuO₂/C has improved activity to produce a 46.94 mA cm⁻² compared with CuO/C (21.55 mA cm⁻²) at 1.7 V vs. RHE. The overall mass activity comparison of CuO/C and CuO/RuO₂/C is provided in Fig. S14. The reason for the robust activity of these catalysts toward OER can be illustrated using C_{dl} values obtained with CV profiles at different scan rates in the anodic non-Faradaic portion, as depicted in Fig. S15. At 0.15 V vs. Hg/HgO, the

experimentally determined C_{dl} value was 1.8 and 7.4 mF cm⁻² for CuO/C and CuO/RuO₂/C, which is theoretically proportional to ECSA, as presented in Fig. 7f. The maximum ECSA was obtained for CuO/RuO₂/C (0.084 mF cm⁻²) compared with CuO/C (0.020 mF cm⁻²). These results justify that introducing low Ru ion content for the formation of RuO₂ greatly influences the number of active sites in the structure. Moreover, the CuO/RuO₂/C sample showed superior structural and chemical stability during the OER process. Figs. S16 and S17 present the FESEM-EDS mapping and XRD pattern for the CuO/RuO₂/C sample after a successful OER test in a 1.0 M KOH solution.

The electrochemical conversion of FF into FA was performed via electrooxidation in 1.0 M KOH with 50 mM FF. Initially, the interaction and binding of FF onto the surface of the electrocatalyst were investigated via anodic oxidation using LSV curves, as exposed in Fig. 8a. With FF, the oxidation potential of both CuO/C and CuO/RuO₂/C considerably improved. Thus, CuO/C and CuO/RuO₂/C tend more toward FF oxidation than water oxidation in an alkaline medium. Fig. 8b shows that the current response was high for CuO/C and CuO/RuO₂/C at the low potential portion and reached 10 mA cm⁻² at 1.562 and 1.536 V vs. RHE, respectively. Compared to simple water oxidation, FOR is advantageous since it is kinetically and thermodynamically favorable. As shown in Fig. 8a, the organic molecule oxidizes at the electrode surface in the low potential region; however, at high potential, the material would easily be involved in oxidizing water. Thus, there is a possibility that charge dispensation during FOR affects the FE of the reaction. FF generated FA via continuous bulk electrolysis at 1.72 V vs. RHE. The reaction progress was monitored via HPLC by measuring the analyte every 30 min. The results are given in Fig. 8c, where CuO/RuO₂/C shows better FF conversion up to 13.28 mM than that up to 12.68 mM for CuO/C at the end of 120 min. The outperforming CuO/RuO₂/C was tested in a potential series (1.526–1.726 V vs. RHE) to optimize the selective potential, and the results are given in Fig. S18. Similarly, the decrease in the FF concentration for CuO/C (22.94 mM) and CuO/RuO₂/C (25.38 mM) was evident during electrooxidation, as revealed in Fig. 8d and Fig. S19. To gain a better understanding of the conversion of FF into FA, we have provided original image results obtained through HPLC in Fig. S20. Further, the conversion efficiency of FF into FA over CuO/C and CuO/RuO₂/C was estimated by comparing CB, FE, and selectivity parameters. During the FF electrooxidation, the CB of CuO/C and CuO/RuO₂/C is 71.54 % and 77.56 %, respectively, as shown in Fig. 8e. Thus, both electrocatalysts showed considerable efficiency in converting FF into FA. The FE of CuO/C and CuO/RuO₂/C at 1.726 V vs. RHE is 49.05 % and 17.61 %, respectively (Fig. 8e). The lowest FE observed in CuO/RuO₂/C is mainly owing to the competitive OER involved during electrooxidation. Fig. 8f shows that CuO/RuO₂/C has the highest selectivity of 54.4 % to deliver FA compared to CuO/C (47.4 %). The above results show that the FF interaction on CuO/RuO₂/C boosted the FF electrooxidation to form FA [76].

Considering the impressive performance of CuO/RuO₂/C catalyst to HER and OER, we developed a two-electrode overall water splitting (OWS) configuration in a conventional H-cell setup with a cell configuration of CuO/RuO₂/C||CuO/RuO₂/C. Further, the LSV study was performed in 1.0 M KOH, and the fabricated CuO/RuO₂/C||CuO/RuO₂/C cell showed a voltage of 1.97 V to provide 10 mA cm⁻². The recorded LSV curve for OWS is given in Fig. S21. Because CuO/C and CuO/RuO₂/C performed well in FHR and FOR, these samples were employed to convert FF into FA and FFA using the CuO/RuO₂/C||CuO/C setup in 1.0 M KOH with and without 50 mM FF. During the LSV study, the electrode material required a 2.1 V to generate 10 mA cm⁻², as depicted in Fig. S22. Interestingly, the cell voltage has decreased to 1.99 V in the presence of FF. As a result, these samples showed evident selectivity to simultaneously convert FF into value-added FA and FFA products.

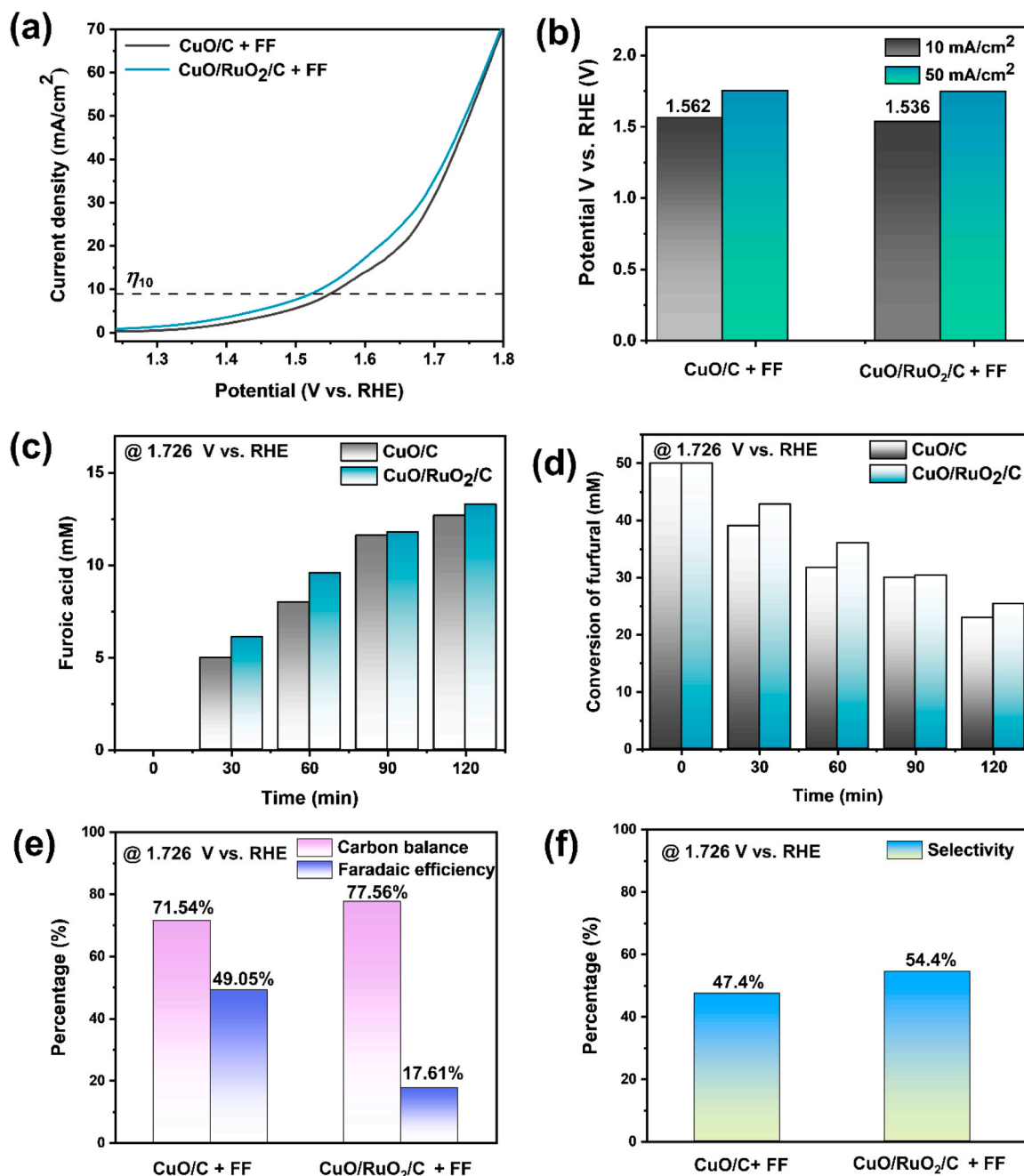


Fig. 8. (a) Polarization curve obtained during FOR over CuO/C and CuO/RuO₂/C with 50 mM FF, (b) potential of each electrocatalyst to attain 10 and 50 mA cm⁻², (c) FA formation at 1.72 V vs. RHE, (d) the conversion of 50 mM FF using the CuO/C and CuO/RuO₂/C electrocatalyst at 1.72 V vs. RHE, (e–f) CB, FE, and selectivity of electrocatalyst for FA formation.

3.4. In situ/operando electrochemical-Raman spectroscopic analysis during HER and OER

The complete mechanism of HER and OER can be understood via performing in situ/operando EC-Raman spectroscopy. The schematic representation of the in situ/operando EC-Raman cell setup is given in Fig. S23. Electrochemical HER (reduction) was initially performed for the best-performing CuO/RuO₂/C in 0.1 M KOH. Before performing in situ/operando EC-Raman analysis, the Raman spectrum of CuO/RuO₂/C electrocatalyst was recorded under 0.1 M KOH without applying cathodic potential. Fig. 9a indicates that the material vibrational mode intensity drastically decreased in a KOH medium. However, the Raman spectrum of CuO/RuO₂/C was able to record. Herein, the vibrational peak corresponding to the Cu–O stretching mode of CuO (♣) is detected

at 299, 347, and 611 cm⁻¹. A constant shift of ~19 cm⁻¹ in the vibrational modes for CuO was observed between the ex situ and in situ recorded Raman spectrum due to the CuO structure bond length change while interacting with KOH [77]. Along with the CuO vibrational peaks, the RuO₂ (♣) nanostructure exhibits a low-intensity vibrational peak at 630 cm⁻¹. Under the open circuit potential (OCP), the catalyst did not undergo any changes and retained its primary phase structure. Upon applying a cathodic potential of -0.2 V vs. RHE, an additional low-intensity peak was recorded at ~416 cm⁻¹ apart from CuO [78]. Interestingly, the emerging peak is associated to the vibrational stretching modes in the Cu–O–Cu of the Cu₂O (♣) nanostructure. Further, increasing the potential up to -1.2 V vs. RHE, the peak formed at 416 cm⁻¹ was gradually increased, indicating that CuO (♣) can undergo a phase transformation at the electrode/electrolyte interface.

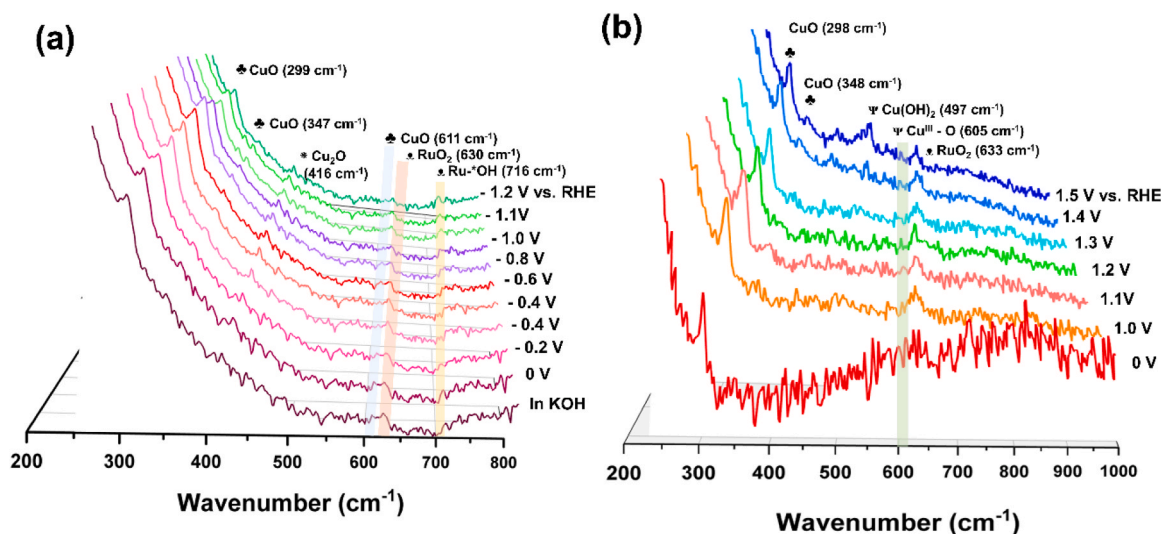


Fig. 9. The in situ/operando EC-Raman spectra of CuO/RuO₂/C during (a) HER and (b) OER in 0.1 M KOH.

Similarly, the peak intensity of RuO₂ (♣) gradually decreased as the cathodic potential increased. Li et al. explained that the intensity lowering of RuO₂ indicates that Ru(IV) valence state might reduce into Ru(II) state. Besides, RuO₂ could interact with the electrolyte to form intermediate *OH species. The formation of the intermediate was faintly recorded at 716 cm⁻¹. Hence, during the cathodic potential, H₂ adsorbs on the surface of *RuO₂ and desorbs after the reaction. Considering this structural orientation, RuO₂ is crucial in converting H⁺ to H₂. Furthermore, Ru is a noble group metal (M), and the strength of the M–H bond and Gibbs free energy (ΔG_H) is very close to the Pt–H bond strength. Thus, Ru and CuO in the composite structure are crucial to produce H₂ [79].

To determine the reaction intermediates during OER, we subjected the freshly prepared electrocatalyst of CuO/RuO₂/C to a constant anodic potential. Under the applied anodic potential (0–1.5 V vs. RHE), these materials undergo an electrooxidation process, as displayed in Fig. 9b. The major characteristic peaks of the sample were diminished when CuO/RuO₂/C was placed in 0.1 M KOH. During the electrooxidation process at OCP, the structural behavior of the material did not change. However, CuO/RuO₂/C exhibits different vibrational modes corresponding to the stretching modes of CuO and RuO₂ under an applied potential. Moreover, the peak intensity of RuO₂ was suppressed in the 0.1 M KOH electrolyte. However, an A_{1g} Raman mode was detected at 633 cm⁻¹, depicting the occurrence of RuO₂ in the heterostructure [80]. Upon further electrooxidation, the CuO nanostructure interacts with the ⁻OH to deliver Cu(OH)₂ or Cu–OOH states [66]. A new hydroxide peak was formed at 497 cm⁻¹ in the potential region between 1.4 and 1.5 V vs. RHE. During oxidation, the material undergoes surface phase transformation, facilitating O₂ evolution. In addition to the CuO oxidation state change, another intermediate was identified during electrooxidation. At high potentials (1.2–1.5 V vs. RHE), a peak shift was observed with a new peak emerging at ~605 cm⁻¹ because CuO endured a transformative Cu^{III}–O oxidation state during oxidation in the KOH medium. Deng et al. recently reported the role of metastable Cu^{III} oxide (ψ) species in OER. Furthermore, the investigation revealed that Cu^{III} oxide was detected only on CuO and Cu(OH)₂ electrodes. Thus, the peak positioned at 605 cm⁻¹ in the sample strongly suggests that the additional peak represents the catalytic active Cu-based species in the oxidation [81]. Similarly, RuO₂ exposes the active site for efficient O₂ generation during electrooxidation via the HOO* intermediate, which is considered the RDS for all metal oxide surfaces. Identifying these intermediates for Ru using the Raman spectrum was quite challenging due to the low vibrational mode intensity of these materials under a KOH medium. However, we could observe that improving the activity of the

electrocatalyst in the presence of RuO₂ (♣) is validates of the role of RuO₂ in OER. Several DFT studies on RuO₂ confirm the intermediate phase structure as M–OOH, as observed similarly for the CuO nanostructure [82]. Recently, Fang and Liu kinetically discovered that RDS for the O₂ evolution on the surface of RuO₂ involves (110) plane, aiding water dissociation with subsequent HOO* formation [83]. Thus, endorse the formation of the M*–OOH intermediate is the RDS for electrooxidation.

4. DFT calculations on furan-analog conformers and their stability

DFT studies were executed in the Gaussian 16 package to study the conformational analysis of FF, FA, and FFA isomers via quantum chemical calculations, validated with the experimental results. Fig. 10 presents the stable conformers of these isomers with respect to the total electronic energy of the FF, FA, and FFA global minimum structure attained by the B3LYP/6–311++G(d,p) process under vacuum. The effect of the H-bond on the stable structure and electronic assets of these isomers is investigated. Among the isomers, the flexible nature of the H-bond forms more stable conformers with these isomers than with other molecules, as mentioned in Fig. 10. Specifically, the vibrational frequency analysis of the geometry optimization was performed with different starting geometries to discriminate the stationary points from the saddle points. Only real frequencies were noticed in the selected isomers.

FF has two isomers with different interactions owing to the nature of the elements in the structure. However, the strong H-bond between the O₁–H₄ (2.543 Å) and O₂–H₃ (3.051 Å) in FF_1 has the lowest energy with the highest stability structure compared to FF_2. Furthermore, FA exhibits four conformers with very similar chemical environments, confirming that a stronger H-bond is vital in the FA_1 (2.295 Å for O₂–H₄) isomer than other possible isomers. In addition, FFA_3 (2.780 Å for O₁–H₄) is a more stable conformer than that of the FFA_1 (2.12 kcal mol⁻¹), FFA_2 (0.96 kcal mol⁻¹) and FFA_4 (1.51 kcal mol⁻¹) isomers. These structures are optimized using molecular polarizability, dipole interactions, the steric hindrance effect, and the orientation of the molecules. However, this has been confirmed by the strong H-bond intramolecular interaction in these stable isomers of the molecules.

It is well-known that the adsorption of reactants on the catalyst surface plays a vital role in the performance of the desired electrochemical redox reactions. Herein, FF must adsorb onto CuO/C and CuO/RuO₂/C in order to be converted into FFA as a hydrogenation product

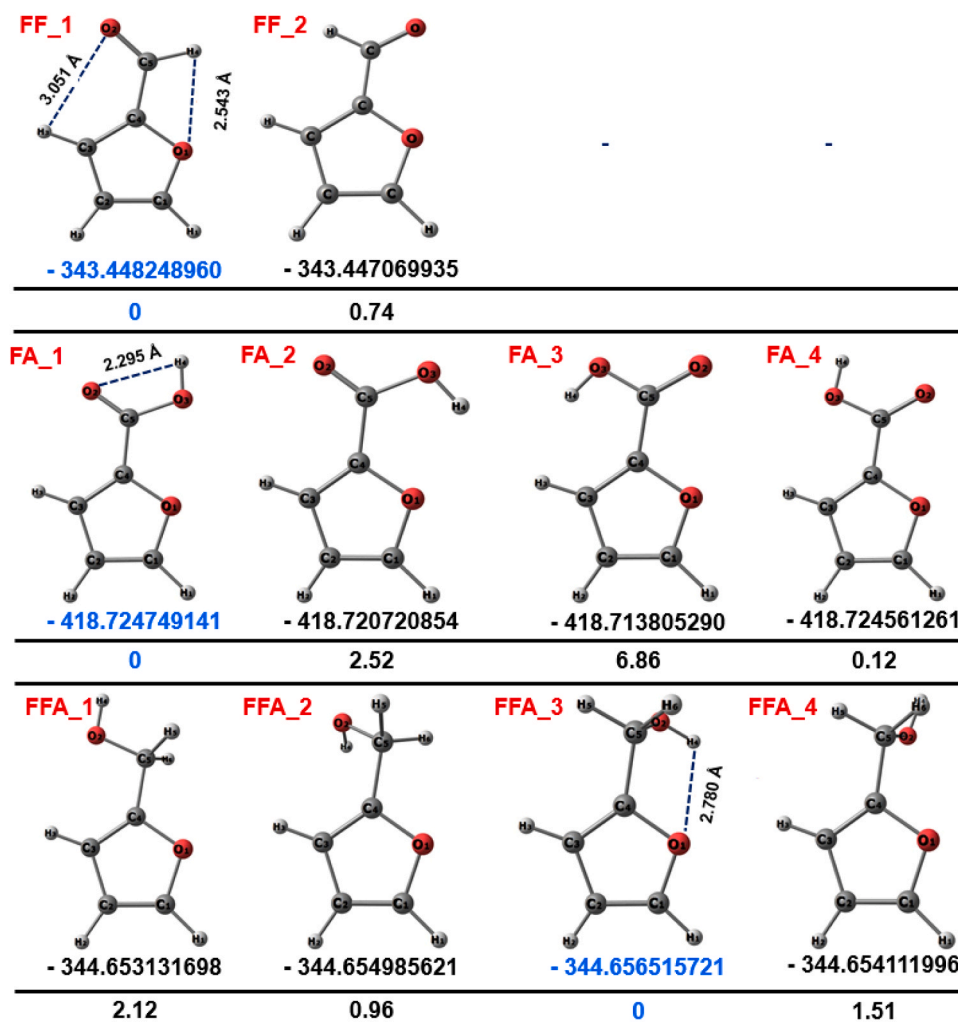


Fig. 10. Conformational analysis of the selected furan-analog isomers.

and FA as an oxidation product, respectively. From in situ Raman studies, the formation of $M^* - H$ and $M^* - OOH$ are responsible for efficient hydrogenation and oxidation reactions, therefore, hydride ion (H^-) and hydroxyl group (OH^-) takes place from the catalyst surface. The carbonyl group of FF showed the highest tendency to interact with the catalyst via the $\eta^1(O)$ -aldehyde conformation because the interaction of the catalyst site with the $C=C$ of the furan ring is weak as they are involved in aromaticity. According to the DFT calculations, the low energy conformer (FF_1) adsorbs onto the electrocatalyst surface with η^1 of the carbonyl oxygen as its H-bonding is weaker, allowing it to form a haptic bond at the defect site. This means the terminal O atom (carbonyl oxygen) of FF is adsorbed onto the O vacancies of the electrocatalyst surface, forming a chemical bond between FF and the active sites of the catalyst. Additionally, the DFT calculations revealed that the stable conformer of the products such as FFA and FA are FFA_3 and FA_1, respectively. It is noteworthy to observe in FA_1 and FF_1, the O1 and O2 are trans to the C₄ and C₅, whereas in FFA_3 they are in the cis position. This can be attributed to the denaturation of $C=O$ and its sp^2 hybridization, which can lead to the change in the geometry of the C₅-atom from planar to T_d . This offers better stability by forming H-bonding, as mentioned in FFA_3.

5. Conclusion

We have systematically developed MOF-derived metal oxides, such as CuO/C and CuO/RuO₂/C, using PLAL. Then, the fabricated

electrocatalysts were successfully employed for the sustainable and innovative conversion of biomass-derived FF into FFA and FA under electrochemical reduction and oxidation, respectively. Initially, CuO/C and CuO/RuO₂/C showed excellent electrochemical activity toward HER and OER. However, CuO/RuO₂/C exhibits the lowest overpotential (η_{10}) of 108 and 346 mV during HER and OER. The electrooxidation of FF on the CuO/RuO₂/C surface proceeds majorly by forming FA with the highest selectivity of $\sim 54.4\%$ and CB of $\sim 77.56\%$ at 1.726 V vs. RHE. Interestingly, CuO/C exhibited better FHR performance for converting FF into FFA than that for CuO/RuO₂/C. Comparatively, CuO/C possessed the highest selectivity (60.0 %) and FE (49.05 %). Furthermore, proton-electron coupled transfer and FHR were inclusively illustrated via the structural reorientation of the CuO/C electrocatalyst. Moreover, the structural understanding of the mechanistic intermediate steps leading to oxidation and reduction of the electrocatalyst was inspected via in situ/operando EC-Raman spectroscopy. Finally, electrochemical routes for valorizing FF molecules deliver sustainable routes to generate value-added chemicals and fuels.

CRediT authorship contribution statement

Shreyanka Shankar Naik - conceptualization, investigation, and data curation; **Jayaraman Theerthagiri** - conceptualization, investigation, writing - review & editing; **Ahreum Min** - Investigation, Reviewing and Editing; **Cheol Joo Moon** - Investigation, Reviewing and Editing; **Seung Jun Lee** - Investigation, Reviewing and Editing; **Myong**

Yong Choi - supervision, funding acquisition, project administration, review & editing.

Declaration of Competing Interest

The authors declare that they have no known competing financial interests or personal relationships that could have appeared to influence the work reported in this paper.

Data availability

Data will be made available on request.

Acknowledgments

This research was supported by Korea Basic Science Institute (National research Facilities and Equipment Center) grant funded by the Ministry of Education. (No. 2019R1A6C1010042, 2021R1A6C103A427). The authors acknowledge the financial support from National Research Foundation of Korea (NRF), (2022R1A2C2010686, 2022R1A4A3033528, 2021R111A1A01060380, 2019H1D3A1A01071209).

Appendix A. Supporting information

Supplementary data associated with this article can be found in the online version at [doi:10.1016/j.apcatb.2023.123164](https://doi.org/10.1016/j.apcatb.2023.123164).

References

- J. Li, R. Yang, S. Xu, C. Zhou, Y. Xiao, C. Hu, D.C.W. Tsang, Biomass-derived polyols valorization towards glycolic acid production with high atom-economy, *Appl. Catal. B: Environ.* 317 (2022), 121785, <https://doi.org/10.1016/j.apcatb.2022.121785>.
- W. Fang, A. Riisager, Efficient valorization of biomass-derived furfural to fuel bio-additive over aluminum phosphate, *Appl. Catal. B: Environ.* 298 (2021), 120575, <https://doi.org/10.1016/j.apcatb.2021.120575>.
- A. Halasa, L. Lapinski, I. Reva, H. Rostkowska, R. Fausto, M.J. Nowak, Three conformers of 2-furoic acid: structure changes induced with near-IR laser light, *J. Phys. Chem. A* 119 (2015) 1037–1047, <https://doi.org/10.1021/jp512302s>.
- J. Theerthagiri, K. Karuppasamy, J. Park, N. Rahamathulla, M.L.A. Kumari, M.K. R. Souza, E.S.F. Cardoso, A.P. Murthy, G. Maia, H.-S. Kim, M.Y. Choi, Electrochemical conversion of biomass-derived aldehydes into fine chemicals and hydrogen: a review, *Environ. Chem. Lett.* (2022), <https://doi.org/10.1007/s10311-022-01543-5>.
- T. Begildayeva, J. Theerthagiri, S.J. Lee, A. Min, G.-A. Kim, S. Manickam, M. Y. Choi, Sustainable furfural biomass feedstocks electrooxidation toward value-added furoic acid with energy-saving H₂ fuel production using Pt-decorated Co₃O₄ nanospheres, *Energy Environ. Mater.* (2022), e12563, <https://doi.org/10.1002/eeem2.12563>.
- Y. Cao, T. Noël, Efficient electrocatalytic reduction of furfural to furfuryl alcohol in a microchannel flow reactor, *Org. Process Res. Dev.* 23 (2019) 403–408, <https://doi.org/10.1021/acs.oprd.8b00428>.
- J.N. Chheda, G.W. Huber, J.A. Dumesic, Liquid-phase catalytic processing of biomass-derived oxygenated hydrocarbons to fuels and chemicals, *Angew. Chem. Int. Ed.* 46 (2007) 7164–7183, <https://doi.org/10.1002/anie.200604274>.
- X.H. Chadderdon, D.J. Chadderdon, J.E. Matthiesen, Y. Qiu, J.M. Carraher, J.-P. Tessonnier, W. Li, Mechanisms of furfural reduction on metal electrodes: distinguishing pathways for selective hydrogenation of bioderived oxygenates, *J. Am. Chem. Soc.* 139 (2017) 14120–14128, <https://doi.org/10.1021/jacs.7b06331>.
- J. Li, N. Kornienko, Probing electrosynthetic reactions with furfural on copper surfaces, *Chem. Commun.* 57 (2021) 5127–5130, <https://doi.org/10.1039/d1cc01429c>.
- M. Zhang, Z. Li, Cu/Cu₂O-MC (MC = Mesoporous Carbon) for highly efficient hydrogenation of furfural to furfuryl alcohol under visible light, *ACS Sustain. Chem. Eng.* 7 (2019) 11485–11492, <https://doi.org/10.1021/acssuschemeng.9b01305>.
- M. Ketkaew, S. Assavapanumat, S. Klinyod, A. Kuhn, C. Wattanakit, Bifunctional Pt/Au Janus electrocatalysts for simultaneous oxidation/reduction of furfural with bipolar electrochemistry, *Chem. Commun.* 58 (2022) 4312–4315, <https://doi.org/10.1039/d1cc06759a>.
- G. Fiorentino, M. Ripa, S. Ulgiati, Chemicals from biomass: technological versus environmental feasibility. A review, *Biofuels Bioprod. Bioref.* 11 (2017) 195–214, <https://doi.org/10.1002/bbb.1729>.
- S. Naik Shreyanka, J. Theerthagiri, S.J. Lee, Y. Yu, M.Y. Choi, Multiscale design of 3D metal–organic frameworks (M–BTC, M: Cu, Co, Ni) via PLAL enabling bifunctional electrocatalysts for robust overall water splitting, *Chem. Eng. J.* 446 (2022), 137045, <https://doi.org/10.1016/j.cej.2022.137045>.
- F. Zheng, W. Zhang, X. Zhang, Y. Zhang, W. Chen, Sub-2 nm ultrathin and robust 2D FeNi layered double hydroxide nanosheets packed with 1D FeNi-MOFs for enhanced oxygen evolution electrocatalysis, *Adv. Funct. Mater.* 31 (2021) 2103318, <https://doi.org/10.1002/adfm.202103318>.
- X. Tan, Y. Wu, X. Lin, A. Zeb, X. Xu, Y. Luo, J. Liu, Application of MOF-derived transition metal oxides and composites as anodes for lithium-ion batteries, *Inorg. Chem. Front.* 7 (2020) 4939–4955, <https://doi.org/10.1039/d0qi00929f>.
- K. Wang, J. Sun, H. Yang, Y. Zhang, X. Zhong, Y. Song, F. Hou, Y. Zhang, Z. Zhang, H. Wang, J. Zhu, H. Sun, J. Liang, MOF-derived 3D interconnected amorphous carbon nanowire networks for robust lithium storage, *Microporous Mesoporous Mater.* 348 (2023), 112388, <https://doi.org/10.1016/j.micromeso.2022.112388>.
- H. Saini, N. Srinivasan, V. Šedajová, M. Majumder, D.P. Dubal, M. Otyepka, R. Zboril, N. Kurra, R.A. Fischer, K. Jayaramulu, Emerging MXene@metal–organic framework hybrids: design strategies toward versatile applications, *ACS Nano* 15 (2021) 18742–18776, <https://doi.org/10.1021/acsnano.1c06402>.
- Z. Liang, C. Qu, W. Guo, R. Zou, Q. Xu, Metal–organic frameworks: pristine metal–organic frameworks and their composites for energy storage and conversion (Adv. Mater. 37(2018), Adv. Mater. 30 (2018) 1870276, <https://doi.org/10.1002/adma.201870276>.
- Z. Liang, C. Qu, W. Guo, R. Zou, Q. Xu, Pristine metal–organic frameworks and their composites for energy storage and conversion, *Adv. Mater.* 30 (2018) 1702891, <https://doi.org/10.1002/adma.201702891>.
- S.S. Naik, S.J. Lee, T. Begildayeva, Y. Yu, H. Lee, M.Y. Choi, Pulsed laser synthesis of reduced graphene oxide supported ZnO/Au nanostructures in liquid with enhanced solar light photocatalytic activity, *Environ. Pollut.* 266 (2020), 115247, <https://doi.org/10.1016/j.envpol.2020.115247>.
- T. Begildayeva, J. Theerthagiri, S.J. Lee, Y. Yu, M.Y. Choi, Unraveling the synergy of anion modulation on co electrocatalysts by pulsed laser for water splitting: intermediate capturing by in situ/operando Raman studies, *Small* 24 (2022) 2204309, <https://doi.org/10.1002/sml.202204309>.
- Y. Yu, J. Theerthagiri, S.J. Lee, G. Muthusamy, M. Ashokkumar, M.Y. Choi, Integrated technique of pulsed laser irradiation and sonochemical processes for the production of highly surface-active NiPd spheres, *Chem. Eng. J.* 411 (2021), 128486, <https://doi.org/10.1016/j.cej.2021.128486>.
- Y. Yu, S.S. Naik, Y. Oh, J. Theerthagiri, S.J. Lee, M.Y. Choi, Lignin-mediated green synthesis of functionalized gold nanoparticles via pulsed laser technique for selective colorimetric detection of lead ions in aqueous media, *J. Hazard. Mater.* 420 (2021), 126585, <https://doi.org/10.1016/j.jhazmat.2021.126585>.
- Y. Yu, S.J. Lee, J. Theerthagiri, Y. Lee, M.Y. Choi, Architecting the AuPt alloys for hydrazine oxidation as an anolyte in fuel cell: comparative analysis of hydrazine splitting and water splitting for energy-saving H₂ generation, *Appl. Catal. B: Environ.* (2022), 121603, <https://doi.org/10.1016/j.apcatb.2022.121603>.
- S.S. Naik, S.J. Lee, J. Theerthagiri, Y. Yu, M.Y. Choi, Rapid and highly selective electrochemical sensor based on ZnS/Au-decorated f-multi-walled carbon nanotube nanocomposites produced via pulsed laser technique for detection of toxic nitro compounds, *J. Hazard. Mater.* 418 (2021), 126269, <https://doi.org/10.1016/j.jhazmat.2021.126269>.
- S.J. Lee, Y. Yu, H.J. Jung, S.S. Naik, S. Yeon, M.Y. Choi, Efficient recovery of palladium nanoparticles from industrial wastewater and their catalytic activity toward reduction of 4-nitrophenol, *Chemosphere* 262 (2021), 128358, <https://doi.org/10.1016/j.chemosphere.2020.128358>.
- J. Theerthagiri, K. Karuppasamy, S.J. Lee, R. Shwetharani, H.-S. Kim, S.K.K. Pasha, M. Ashokkumar, M.Y. Choi, Fundamentals and comprehensive insights on pulsed laser synthesis of advanced materials for diverse photo- and electrocatalytic applications, *Light: Sci. Appl.* 11 (2022) 250, <https://doi.org/10.1038/s41377-022-00904-7>.
- Y. Jeong, S. Shankar Naik, Y. Yu, J. Theerthagiri, S.J. Lee, P.L. Show, H.C. Choi, M. Y. Choi, Ligand-free monophase CuPd alloys endow boosted reaction kinetics toward energy-efficient hydrogen fuel production paired with hydrazine oxidation, *J. Mater. Sci. Technol.* 143 (2023) 20–29, <https://doi.org/10.1016/j.jmst.2022.09.043>.
- S. Shankar Naik, J. Theerthagiri, F.S. Nogueira, S.J. Lee, A. Min, G.-A. Kim, G. Maia, L.M.C. Pinto, M.Y. Choi, Dual-cation-coordinated CoFe-layered double-hydroxide nanosheets using the pulsed laser ablation technique for efficient electrochemical water splitting: mechanistic screening by in situ/operando raman and density functional theory calculations, *ACS Catal.* 13 (2023) 1477–1491, <https://doi.org/10.1021/acscatal.2c05017>.
- S.S. Naik, S.J. Lee, S. Yeon, Y. Yu, M.Y. Choi, Pulsed laser-assisted synthesis of metal and nonmetal-codoped ZnO for efficient photocatalytic degradation of Rhodamine B under solar light irradiation, *Chemosphere* 274 (2021), 129782, <https://doi.org/10.1016/j.chemosphere.2021.129782>.
- J. Theerthagiri, K. Karuppasamy, A. Min, D. Govindarajan, M.L.A. Kumari, G. Muthusamy, S. Kheawhom, H.-S. Kim, M.Y. Choi, Unraveling the fundamentals of pulsed laser-assisted synthesis of nanomaterials in liquids: applications in energy and the environment, *Appl. Phys. Rev.* 9 (2022), 041314, <https://doi.org/10.1063/5.0104740>.
- L. Liu, H. Liu, W. Huang, Y. He, W. Zhang, C. Wang, H. Lin, Mechanism and kinetics of the electrocatalytic hydrogenation of furfural to furfuryl alcohol, *J. Electroanal. Chem.* 804 (2017) 248–253, <https://doi.org/10.1016/j.jelechem.2017.09.021>.
- W. Xu, C. Yu, J. Chen, Z. Liu, Electrochemical hydrogenation of biomass-based furfural in aqueous media by Cu catalyst supported on N-doped hierarchically porous carbon, *Appl. Catal. B: Environ.* 305 (2022), 121062, <https://doi.org/10.1016/j.apcatb.2022.121062>.

- [34] Q. Tian, T. Shi, Y. Sha, CuO and Ag₂O/CuO catalyzed oxidation of aldehydes to the corresponding carboxylic acids by molecular oxygen, *Molecules* 13 (2008) 948–957, <https://doi.org/10.3390/molecules13040948>.
- [35] F. Israr, D.K. Kim, Y. Kim, S.J. Oh, K.C. Ng, W. Chun, Synthesis of porous Cu-BTC with ultrasonic treatment: Effects of ultrasonic power and solvent condition, *Ultrason. Sonochem.* 29 (2016) 186–193, <https://doi.org/10.1016/j.ultsonch.2015.08.023>.
- [36] K.-J. Kim, Y.J. Li, P.B. Kreider, C.-H. Chang, N. Wannenmacher, P.K. Thallapally, H.-G. Ahn, High-rate synthesis of Cu-BTC metal-organic frameworks, *Chem. Commun.* 49 (2013) 11518–11520, <https://doi.org/10.1039/c3cc46049e>.
- [37] Y. Cao, L. Wang, C. Wang, D. Su, Y. Liu, X. Hu, Photoelectrochemical determination of malathion by using CuO modified with a metal-organic framework of type Cu-BTC, *Microchim. Acta* 186 (2019) 481, <https://doi.org/10.1007/s00604-019-3597-0>.
- [38] W. Wang, Y. Zhang, J. Zhang, G. Li, D. Leng, Y. Gao, J. Gao, H. Lu, X. Li, Metal-organic framework-derived Cu₂O–CuO octahedrons for sensitive and selective detection of ppb-level NO₂ at room temperature, *Sens. Actuators B: Chem.* 328 (2021), 129045, <https://doi.org/10.1016/j.snb.2020.129045>.
- [39] A. Devadas, S. Baranton, C. Coutanceau, Green synthesis and modification of RuO₂ materials for the oxygen evolution reaction, *Front. Energy Res.* 8 (2020), 571704, <https://doi.org/10.3389/fenrg.2020.571704>.
- [40] K. Dharmalingam, D. Bordoloi, A.B. Kunnumakkara, R. Anandalakshmi, Preparation and characterization of cellulose-based nanocomposite hydrogel films containing CuO/Cu₂O/Cu with antibacterial activity, *J. Appl. Polym. Sci.* 137 (2020) 49216, <https://doi.org/10.1002/app.49216>.
- [41] V. Rao, K. Jhansi, S. Chandralingam, N. Reddy, P. Suvarna, C. Ashok, K. Rao, CuO nanoparticles synthesis and characterization for humidity sensor application, *J. Nanotechnol. Mater. Sci.* 4 (2016) 27, <https://doi.org/10.15436/2377-1372.16.020>.
- [42] H. Wang, R.G. Gordon, R. Alvis, R.M. Ulfig, Atomic layer deposition of ruthenium thin films from an amidinate precursor, *Chem. Vap. Depos.* 15 (2009) 312–319, <https://doi.org/10.1002/cvde.200906789>.
- [43] W. Lestari, D. Ni'maturohman, U. Arrozi, H. Suwarno, Mg²⁺ Doped into electro-synthesized HKUST-1 and their initial hydrogen sorption properties, *IOP Conf. Ser.: Mater. Sci. Eng.* 299 (2018), 012031, <https://doi.org/10.1088/1757-899X/299/1/012031>.
- [44] A. Hajinrouzi, Two ultrasonic applications for the synthesis of nanostructured copper oxide (II), *Ultrason. Sonochem.* 64 (2020), 105020, <https://doi.org/10.1016/j.ultsonch.2020.105020>.
- [45] A.F. Zedan, A.T. Mohamed, M.S. El-Shall, S.Y. AlQaradawi, A.S. AlJaber, Tailoring the reducibility and catalytic activity of CuO nanoparticles for low temperature CO oxidation, *RSC Adv.* 8 (2018) 19499–19511, <https://doi.org/10.1039/c8ra03623c>.
- [46] Y. Lee, J.H. Ahn, S. Shin, S.-H. Jung, H.-S. Park, Y.-G. Cho, D.-G. Lee, H. Kong, J. H. Lee, H.-K. Song, Metal-nitrogen intimacy of the nitrogen-doped ruthenium oxide for facilitating electrochemical hydrogen production, *Appl. Catal. B: Environ.* 303 (2022), 120873, <https://doi.org/10.1016/j.apcatb.2021.120873>.
- [47] J.F. Xu, W. Ji, Z.X. Shen, S.H. Tang, X.R. Ye, D.Z. Jia, X.Q. Xin, Preparation and characterization of CuO nanocrystals, *J. Solid State Chem.* 147 (1999) 516–519, <https://doi.org/10.1006/jssc.1999.8409>.
- [48] J. Chrzanoski, J.C. Irwin, Raman scattering from cupric oxide, *Solid State Commun.* 70 (1989) 11–14, [https://doi.org/10.1016/0038-1098\(89\)90457-2](https://doi.org/10.1016/0038-1098(89)90457-2).
- [49] Y. Xu, K. Chu, Z. Li, S. Xu, G. Yao, P. Niu, F. Zheng, Porous CuO@C composite as high-performance anode materials for lithium-ion batteries, *Dalton Trans.* 49 (2020) 11597–11604, <https://doi.org/10.1039/d0dt02493g>.
- [50] S. Jung, R.A. Senthil, C.J. Moon, N. Tarasenko, A. Min, S.J. Lee, N. Tarasenko, M. Y. Choi, Mechanistic insights into ZIF-67-derived Ir-doped Co₃O₄@N-doped carbon hybrids as efficient electrocatalysts for overall water splitting using in situ Raman spectroscopy, *Chem. Eng. J.* 468 (2023), 143717, <https://doi.org/10.1016/j.cej.2023.143717>.
- [51] A.V. Korotkov, Y.-S. Huang, K.-K. Tiong, D.-S. Tsai, Raman scattering characterization of well-aligned RuO₂ and IrO₂ nanocrystals, *J. Raman Spectrosc.* 38 (2007) 737–749, <https://doi.org/10.1002/jrs.1655>.
- [52] S.M.A. Shibli, M. Ameen Sha, Development and characterization of electro active CeO₂–RuO₂ mixed oxide and its role in alkaline hydrogen evolution reaction, *J. Alloy. Compd.* 749 (2018) 250–261, <https://doi.org/10.1016/j.jallcom.2018.03.274>.
- [53] M.Z. Hussain, Z. Yang, B. van der Linden, W.R. Heinz, M. Bahri, O. Ersen, Q. Jia, R. A. Fischer, Y. Zhu, Y. Xia, MOF-derived multi-heterostructured composites for enhanced photocatalytic hydrogen evolution: deciphering the roles of different components, *Energy Fuels* 36 (2022) 12212–12225, <https://doi.org/10.1021/acs.energyfuels.2c02319>.
- [54] A.Y. Kim, M.K. Kim, K. Cho, J.-Y. Woo, Y. Lee, S.-H. Han, D. Byun, W. Choi, J. K. Lee, One-step catalytic synthesis of CuO/Cu₂O in a graphitized porous C matrix derived from the Cu-based metal-organic framework for Li- and Na-Ion batteries, *ACS Appl. Mater. Interfaces* 8 (2016) 19514–19523, <https://doi.org/10.1021/acsami.6b05973>.
- [55] G. Panzner, B. Egert, H.P. Schmidt, The stability of CuO and Cu₂O surfaces during argon sputtering studied by XPS and AES, *Surf. Sci.* 151 (1985) 400–408, [https://doi.org/10.1016/0039-6028\(85\)90383-8](https://doi.org/10.1016/0039-6028(85)90383-8).
- [56] Ç. Oruç, A. Altındal, Structural and dielectric properties of CuO nanoparticles, *Ceram. Int.* 43 (2017) 10708–10714, <https://doi.org/10.1016/j.ceramint.2017.05.006>.
- [57] W. Lv, L. Li, Q. Meng, X. Zhang, Molybdenum-doped CuO nanosheets on Ni foams with extraordinary specific capacitance for advanced hybrid supercapacitors, *J. Mater. Sci.* 55 (2020) 2492–2502, <https://doi.org/10.1007/s10853-019-04129-9>.
- [58] M.A. Khan, N. Nayan, M.K. Ahmad, C.F. Soon, Surface study of CuO nanopetals by advanced nanocharacterization techniques with enhanced optical and catalytic properties, *Nanomaterials* 10 (2020) 1298, <https://doi.org/10.3390/nano10071298>.
- [59] Y. Wang, Y. Lü, W. Zhan, Z. Xie, Q. Kuang, L. Zheng, Synthesis of porous Cu₂O/CuO cages using Cu-based metal-organic frameworks as templates and their gas-sensing properties, *J. Mater. Chem. A* 3 (2015) 12796–12803, <https://doi.org/10.1039/C5TA01108F>.
- [60] Q. Hu, J. Qin, X.-F. Wang, G.-Y. Ran, Q. Wang, G.-X. Liu, J.-P. Ma, J.-Y. Ge, H.-Y. Wang, Cu-based conductive MOF grown in situ on Cu foam as a highly selective and stable non-enzymatic glucose sensor, *Front. Chem.* 9 (2021), 786970, <https://doi.org/10.3389/fchem.2021.786970>.
- [61] C. Zhao, X. Tang, J. Zhao, J. Cao, Z. Jiang, J. Qin, MOF derived core-shell CuO/C with temperature-controlled oxygen-vacancy for real time analysis of glucose, *J. Nanobiotechnol.* 20 (2022) 1–12, <https://doi.org/10.1186/s12951-022-01715-z>.
- [62] D. Chen, S. Zhao, Z. Qu, N. Yan, Cu-BTC as a novel material for elemental mercury removal from sintering gas, *Fuel* 217 (2018) 297–305, <https://doi.org/10.1016/j.fuel.2017.12.086>.
- [63] S. Hao, L. Yuling, J. Yang, Construction of Cu-BTC by carboxylic acid organic ligand and its application in low temperature SCR denitration, *Sci. Total Environ.* 820 (2022), 152984, <https://doi.org/10.1016/j.scitotenv.2022.152984>.
- [64] P. Wang, H. Liu, Q. Tan, J. Yang, Ruthenium oxide-based nanocomposites with high specific surface area and improved capacitance as a supercapacitor, *RSC Adv.* 4 (2014) 42839–42845, <https://doi.org/10.1039/c4ra07044e>.
- [65] Y.-H. Wang, R.-Q. Li, H.-B. Li, H.-L. Huang, Z.-J. Guo, H.-Y. Chen, Y. Zheng, K.-G. Qu, Controlled synthesis of ultrasmall RuP₂ particles on N, P-codoped carbon as superior pH-wide electrocatalyst for hydrogen evolution, *Rare Met.* 40 (2021) 1040–1047, <https://doi.org/10.1007/s12598-020-01665-1>.
- [66] X. Pang, H. Zhao, Y. Huang, Y. Liu, H. Bai, W. Fan, W. Shi, In situ electrochemical reconstitution of CF–CuO/CeO₂ for efficient active species generation, *Inorg. Chem.* 61 (2022) 8940–8954, <https://doi.org/10.1021/acs.inorgchem.2c01338>.
- [67] R. Rao, A. Dandekar, R.T.K. Baker, M.A. Vannice, Properties of copper chromite catalysts in hydrogenation reactions, *J. Catal.* 171 (1997) 406–419, <https://doi.org/10.1006/jcat.1997.1832>.
- [68] X.-X. Ma, L. Chen, Z. Zhang, J.-L. Tang, Electrochemical performance evaluation of CuO/Cu₂O nanowires array on Cu foam as bifunctional electrocatalyst for efficient water splitting, *Chin. J. Anal. Chem.* 48 (2020) e20001–e20012, [https://doi.org/10.1016/S1872-2040\(19\)61211-9](https://doi.org/10.1016/S1872-2040(19)61211-9).
- [69] L. Zhu, H. Li, Z. Liu, P. Xia, Y. Xie, D. Xiong, Synthesis of the 0D/3D CuO/ZnO heterojunction with enhanced photocatalytic activity, *J. Phys. Chem. C* 122 (2018) 9531–9539, <https://doi.org/10.1021/acs.jpcc.8b01933>.
- [70] Q. Zhang, L. Huang, S. Kang, C. Yin, Z. Ma, L. Cui, Y. Wang, CuO/Cu₂O nanowire arrays grafted by reduced graphene oxide: synthesis, characterization, and application in photocatalytic reduction of CO₂, *RSC Adv.* 7 (2017) 43642–43647, <https://doi.org/10.1039/C7RA07310K>.
- [71] S. Sittithisa, D.E. Resasco, Hydrodeoxygenation of furfural over supported metal catalysts: a comparative study of Cu, Pd and Ni, *Catal. Lett.* 141 (2011) 784–791, <https://doi.org/10.1007/s10562-011-0581-7>.
- [72] S. Liu, Z. Mukadam, S. Scott, S. Sarma, M.-M. Titirici, K. Chan, N. Govindarajan, I. Stephens, G. Kastlunger, Unraveling the reaction mechanisms for furfural electroreduction on copper, (2023). [10.1039/D3EY00040K](https://doi.org/10.1039/D3EY00040K).
- [73] W. Wang, Z. Wang, Y. Hu, Y. Liu, S. Chen, A potential-driven switch of activity promotion mode for the oxygen evolution reaction at Co₃O₄/NiO_xH_y interface, *eScience* 2 (2022) 438–444, <https://doi.org/10.1016/j.esci.2022.04.004>.
- [74] W. Zhu, X. Zuo, X. Zhang, X. Deng, D. Ding, C. Wang, J. Yan, X. Wang, G. Wang, MOFs-derived CuO–Fe₃O₄@C with abundant oxygen vacancies and strong Cu–Fe interaction for deep mineralization of bisphenol A, *Environ. Res.* 228 (2023), 115847, <https://doi.org/10.1016/j.envres.2023.115847>.
- [75] X.-Z. Ren, X.-H. Li, Y.-J. Peng, G.-Z. Wang, J. Yin, X.-C. Zhao, W. Wang, X.-B. Wang, FeNiS₂/reduced graphene oxide electrocatalysis with reconstruction to generate FeNi oxo/hydroxide as a highly-efficient water oxidation electrocatalyst, *Rare Met.* 41 (2022) 4127–4137, <https://doi.org/10.1007/s12598-022-02104-z>.
- [76] S. Kar, Q.-Q. Zhou, Y. Ben-David, D. Milstein, Catalytic furfural/5-hydroxymethyl furfural oxidation to furoic acid/furan-2,5-dicarboxylic acid with H₂ production using alkaline water as the formal oxidant, *J. Am. Chem. Soc.* 144 (2022) 1288–1295, <https://doi.org/10.1021/jacs.1c10908>.
- [77] E. Flores, P. Novák, E.J. Berg, In situ and operando Raman spectroscopy of layered transition metal oxides for Li-ion battery cathodes, *Front. Energy Res.* 6 (2018) 82, <https://doi.org/10.3389/fenrg.2018.00082>.
- [78] C. Zhan, F. Dattila, C. Rettenmaier, A. Bergmann, S. Kühl, R. García-Muelas, N. López, B.R. Cuenya, Revealing the CO coverage-driven C–C coupling mechanism for electrochemical CO₂ reduction on Cu₂O nanocubes via operando Raman spectroscopy, *ACS Catal.* 11 (2021) 7694–7701, <https://doi.org/10.1021/acscatal.1c01478>.
- [79] D.H. Kweon, M.S. Okyay, S.-J. Kim, J.-P. Jeon, H.-J. Noh, N. Park, J. Mahmood, J.-B. Baek, Ruthenium anchored on carbon nanotube electrocatalyst for hydrogen production with enhanced Faradaic efficiency, *Nat. Commun.* 11 (2020) 1278, <https://doi.org/10.1038/s41467-020-15069-3>.
- [80] S.Y. Mar, C.S. Chen, Y.S. Huang, K.K. Tiong, Characterization of RuO₂ thin films by Raman spectroscopy, *Appl. Surf. Sci.* 90 (1995) 497–504, [https://doi.org/10.1016/0169-4332\(95\)00177-8](https://doi.org/10.1016/0169-4332(95)00177-8).
- [81] Y. Deng, A.D. Handoko, Y. Du, S. Xi, B.S. Yeo, In situ Raman spectroscopy of copper and copper oxide surfaces during electrochemical oxygen evolution reaction:

- identification of Cu^{III} oxides as catalytically active species, ACS Catal. 6 (2016) 2473–2481, <https://doi.org/10.1021/acscatal.6b00205>.
- [82] Y. Hu, X. Luo, G. Wu, T. Chao, Z. Li, Y. Qu, H. Li, Y. Wu, B. Jiang, X. Hong, Engineering the atomic layer of RuO₂ on PdO nanosheets boosts oxygen evolution catalysis, ACS Appl. Mater. Interfaces 11 (2019) 42298–42304, <https://doi.org/10.1021/acsami.9b16492>.
- [83] Y.-H. Fang, Z.-P. Liu, Mechanism and tafel lines of electro-oxidation of water to oxygen on RuO₂(110), J. Am. Chem. Soc. 132 (2010) 18214–18222, <https://doi.org/10.1021/ja1069272>.